**FACULTY**
**OF MATHEMATICS**
**AND PHYSICS**
**Charles University**

# BACHELOR THESIS

Tomáš Klásek

# Semi-inclusive DIS studies at COMPASS experiment

Department of Low-Temperature Physics

| | |
|---|---|
| Supervisor of the bachelor thesis: | Mgr. Michael Pešek, Ph.D. |
| Study programme: | Physics |
| Study branch: | FP |

Prague 2023

I declare that I carried out this bachelor thesis independently, and only with the cited sources, literature and other professional sources. It has not been used to obtain another or the same degree.

I understand that my work relates to the rights and obligations under the Act No. 121/2000 Sb., the Copyright Act, as amended, in particular the fact that the Charles University has the right to conclude a license agreement on the use of this work as a school work pursuant to Section 60 subsection 1 of the Copyright Act.

In ............ date ............ ....................................

Author's signature

I would like to take a moment to express my heartfelt gratitude to the people who made this achievement possible. Firstly, I would like to thank my supervisor Michael Pešek and consultant Jan Matoušek, for their invaluable guidance, support, and encouragement throughout my research journey. Their expertise and passion for the subject have been truly inspiring, and I feel privileged to have worked under their supervision.

I am also deeply grateful to Artem Ivanov, who helped me prepare the codes for the final analysis and was always available to answer my tiring questions. Our frequent meetings were very helpful in clarifying complex issues, and his expertise and dedication were instrumental in the success of this project.

I would also like to extend my appreciation to my fluffy cute rabbit Billy, who provided much-needed comfort and companionship during many late nights of work. My family and friends have been a constant source of encouragement and support, and I am deeply grateful for their love and understanding.

Finally, I would like to thank the COMPASS experiment team for providing me with the opportunity to be a part of this exciting research project. This thesis is a result of their hard work and dedication, and I am honoured to have contributed to this important work. Thank you all for being a part of this journey with me.

Title: Semi-inclusive DIS studies at COMPASS experiment

Author: Tomáš Klásek

Department: Department of Low-Temperature Physics

Supervisor: Mgr. Michael Pešek, Ph.D., Department of Low-Temperature Physics

Abstract: This bachelor's thesis focuses on exploring the SIDIS data collected at the COMPASS experiment in 2022. The beginning of the thesis briefly summarises the theory, including the SIDIS, the definition of the kinematic variables and the TMD-PDF functions, and the layout of the COMPASS experiment with its main components, which were used in 2022 data taking. The following part comprises target analysis, in which the target density is visualised and its position determined. In the last section, the bad spill analysis is used to investigate the stability of data, which is crucial for the measurement of traverse spin asymmetries. A description of the procedure, a comparison of different selection criteria and results for two data-taking periods are presented.

Keywords: DIS COMPASS TMD nucleon structure

# Contents

# Introduction

Elementary particle physics underwent rapid development during the 20th century. It seeks to address the fundamental nature of matter and its constituent components. In 1964, Gell-Mann and Zweig independently predicted that all hadrons comprise even smaller particles called *quarks* [1]. Subsequently, the SLAC-MIT experiment data revealed evidence for the existence of smaller constituents inside protons. This empirical proof supports the theoretical prediction of the quarks [2]. It became clear that nucleons can be described as complex dynamic systems of many partons. This model was later enhanced to incorporate transverse momentum dependent (TMD) functions in order to describe processes where parton transverse momentum plays a role, like semi-inclusive DIS.

The COMPASS experiment was designed to study many aspects of nucleon spin structure. Measurements on polarised proton and deuteron targets gave the most precise results of the transversity and Sivers PDFs. In 2022 COMPASS collected additional data with polarised deuteron target in order to have comparable statistics on protons and deuterons to allow for further precision of d-quark related PDFs.

This thesis has two main subjects. The first one is to examine the target density and position by studying the distribution of vertices and beam tracks over the whole target. The second subject is bad spill analysis, which is needed to select stable data for further analysis.

The thesis is organised as follows: the first Chapter contains the theoretical overview, which functions as a basis for the following chapters focusing on analysis. The second Chapter comprises familiarisation with the COMPASS experiment and its main components. The target position and density of all three target cells are analysed in Chapter 3. It also contains depictions of vertices and beam tracks distributions. Chapter 4 describes the details of the bad spill analysis, the possible methods of processing the data sets and the comparison of the results.

All of the mentioned results were discussed in the COMPASS transversity and analysis meetings. Several plots were also presented at the DIS2023 [3] conference.

# 1. Theoretical introduction

## 1.1 Deep inelastic scattering

Deep inelastic scattering (DIS) is a method of investigating the structure of the nucleon $N$ with momentum $P$ using a high-energy lepton $\ell$ with momentum $l$. The basic equation of such a process can be described as [4]

$$\ell(l) + N(P) \to \ell(l') + X, \tag{1.1}$$

where $\ell(l')$ is the scattered lepton with momentum $l'$ and $X$, is an unobserved hadronic state, which represents produced hadrons [5, 6]. There are three kinds of DIS. It is called inclusive if only the scattered lepton is observed, semi-inclusive if both the scattered lepton and at least one part of $X$ are observed or exclusive if the $X$ is completely reconstructed [7, 6].

## 1.2 Semi-inclusive deep inelastic scattering

As previously stated, semi-inclusive DIS refers to DIS, where both the scattered lepton $l'$ and part of the remainder $X$ denoted $h$ are observed. It can be described by an equation [6]

$$\ell(l) + N(P) \to \ell(l') + h(P_h) + X, \tag{1.2}$$

where $P_h$ is the momentum of $h$ [6].

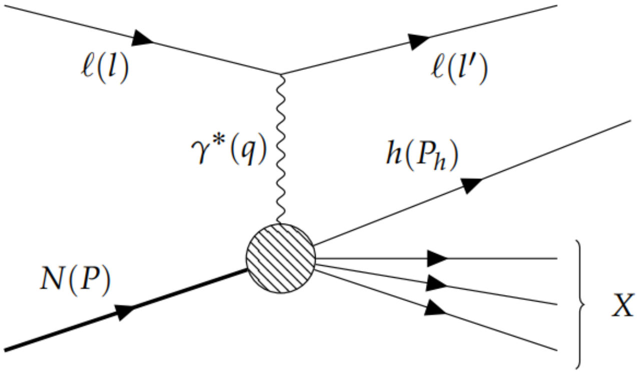

Figure 1.1: Feynman diagram of the semi-inclusive deep inelastic scattering in one photon exchange approximation [6]

Figure 1.1 shows a Feynman diagram of SIDIS. Kinematic equations describing the whole process can be constructed using the nucleon's mass and the momenta of lepton before and after scattering. Here is the list of the formulae [7, 8]:

- Negative squared 4-momentum transfer

$$Q^2 = -q^2 = -(l - l')^2 \tag{1.3}$$

- Bjorken scaling variable

$$x = \frac{Q^2}{2P \cdot q} \tag{1.4}$$

- Squared invariant mass of the photon-nucleon system

$$W^2 = (P + q)^2 \tag{1.5}$$

- The inelasticity

$$y = \frac{P \cdot q}{P \cdot l} = \frac{E_{lab} - E'_{lab}}{E_{lab}} \tag{1.6}$$

Further, the Gamma-Nucleon System (GNS) is defined; see 1.2. It is a centre of mass system in the reference frame of the virtual photon and target nucleon defined as follows: the direction of the virtual photon defines the $z$ axis, the $x$ axis is perpendicular to $z$ and lies in the plane determined by the momenta of $l$ and $l'$, and the $y$ axis is fixed so that $xyz$ is an orthogonal system [6].

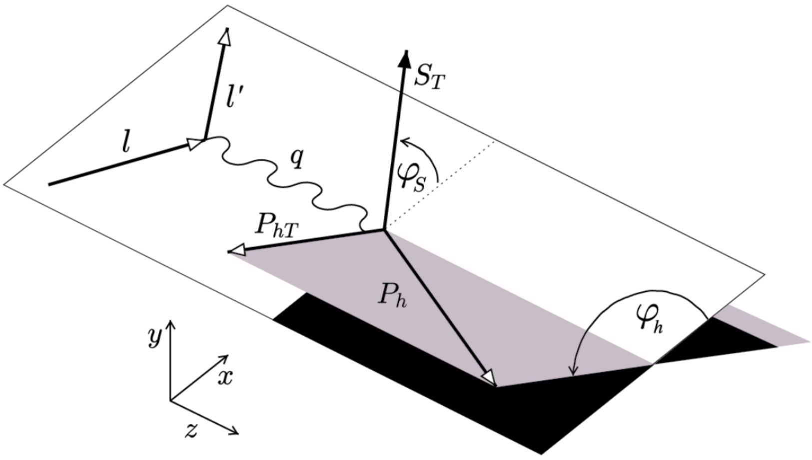

Figure 1.2: The scheme of the Gamma-Nucleon System (GNS)

In the GNS, more kinematic variables are defined. One of them is $\boldsymbol{P}_{hT}$, the hadron momentum perpendicular to the virtual photon momentum, given by formula [6]

$$\boldsymbol{P}_{hT} = \boldsymbol{P}_h - \frac{(\boldsymbol{P}_h \cdot \boldsymbol{q})\boldsymbol{q}}{|\boldsymbol{q}^2|}. \tag{1.7}$$

The relation describing the fractional energy of the observed final state hadron is given by [8]

$$z = \frac{P \cdot P_h}{P \cdot q}. \tag{1.8}$$

Finally, the lepton-hadron cross-section for SIDIS in a single photon exchange approximation in addition to approximation $Q^2 \gg 2Mx$ can be written as [9]

$$
\begin{aligned}
&\frac{\mathrm{d}\sigma_{SIDIS}}{\mathrm{d}x\mathrm{d}y\mathrm{d}z\mathrm{d}\phi_S\mathrm{d}\phi_h\mathrm{d}\boldsymbol{P}_{hT}^2} = \frac{\alpha^2}{xyQ^2}\Big(1+\frac{\gamma^2}{2x}\Big) \\
&\times\Bigg\{\frac{2-2y+y^2}{2}F_{UU,T} + (1-y)F_{UU,L} + (2-y)\sqrt{1-y}\cos\phi_h F_{UU}^{\cos\phi_h} \\
&\quad +(1-y)\cos(2\phi_h)F_{UU}^{\cos(2\phi_h)} + \lambda y\sqrt{1-y}\sin\phi_h F_{LU}^{\sin\phi_h} \\
&+|\boldsymbol{S}_T|\Big[\sin(\phi_h-\phi_S)\Big(\frac{2-2y+y^2}{2}F_{UT,T}^{\sin(\phi_h-\phi_S)} + (1-y)F_{UT,L}^{\sin(\phi_h-\phi_S)}\Big) \\
&\quad +(1-y)\Big(\sin(\phi_h+\phi_S)F_{UT}^{\sin(\phi_h+\phi_S)} + \sin(3\phi_h-\phi_S)F_{UT}^{\sin(3\phi_h-\phi_S)}\Big)\Big] \\
&+\lambda|\boldsymbol{S}_T|\Big[\frac{2y+y^2}{2}\cos(\phi_h-\phi_S)F_{LT}^{\cos(\phi_h-\phi_S)} + y\sqrt{1-y}\cos\phi_S F_{LT}^{\cos\phi_S} \\
&\quad +y\sqrt{1-y}\cos(2\phi_h-\phi_S)F_{LT}^{\cos(2\phi_h-\phi_S)}\Big]\Bigg\},
\end{aligned}
\tag{1.9}
$$

where $\alpha$ is the fine structure constant, $\boldsymbol{S}$ is the covariant spin vector of the target, $\gamma = 2Mx/Q$ and $F_{XY,Z}$ are the structure functions dependent on $x, Q^2, z$ and $\boldsymbol{P}_{hT}^2$. The first two lower subscripts denote the polarisation of the beam and the target, and the third one is the polarisation of the virtual photon.

The cross-section can also be expressed in the form of asymmetries using formula [10, 11]

$$
A_{BeamTarget}^{f(\Phi_i)} = \frac{F_{BeamTarget}^{f(\Phi_i)}}{F_{UU,T} + \epsilon F_{UU,L}},
\tag{1.10}
$$

where $A^{f(\Phi_i)}$ denotes the desired asymmetry,$f(\Phi_i)$ is one of the angular dependencies, 'Beam' and 'Target' represent the corresponding polarisations (U, L or T). Kinematic variable $\epsilon$ is defined as [10]

$$
\epsilon = \frac{1-y-\gamma^2y^2/4}{1-y+y^2/2+\gamma^2y^2/4}.
\tag{1.11}
$$

## 1.3 Parton model and Transverse Momentum Dependent Parton Distribution Functions

The parton model uses the infinite momentum frame approximation, in which the strong force binding the nucleon together appears negligible. The hadron can then be described as a collection of massless point-like particles, partons. The parton distribution functions (PDF) are used for this description.

There are three PDFs necessary to describe the nucleon - the number density (ordinary PDF), helicity (longitudinally polarised nucleon) and transversity (transverse polarised nucleon). These are called collinear PDFs. An example of recent extraction of the number density and helicity is shown in figure 1.3.

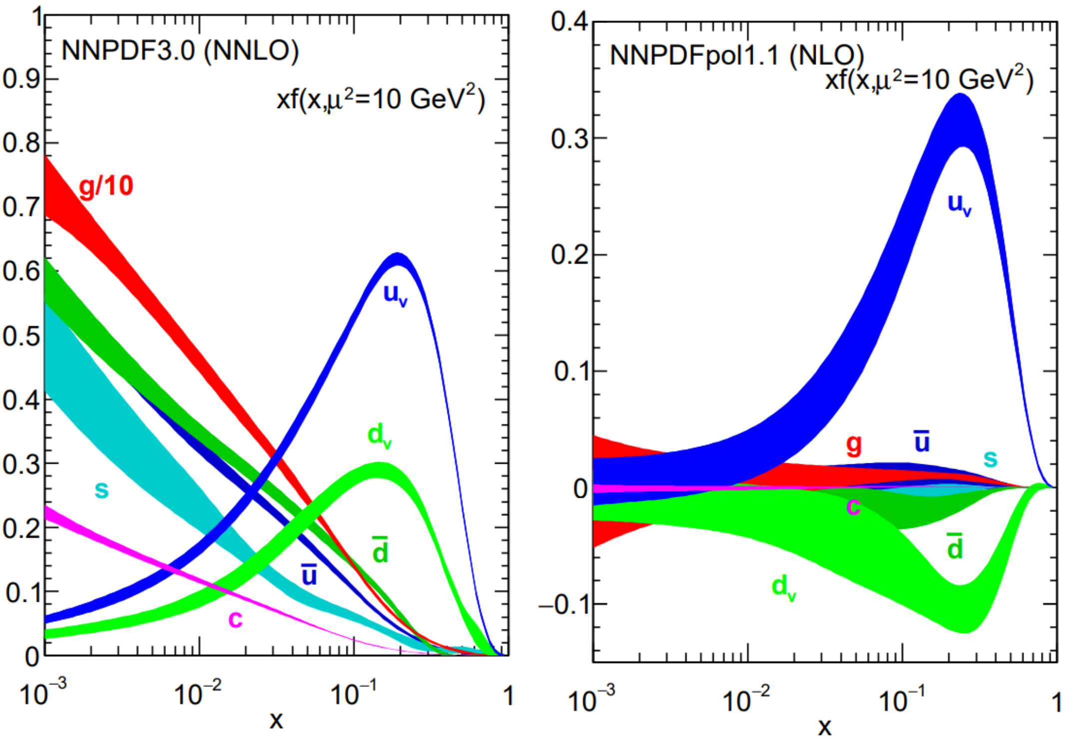

Figure 1.3: An example of extraction of the collinear PDFs from global data by NNPDF [12]

However, these PDFs describe the distribution of quarks within the hadron only in the longitudinal momentum space. If the transverse momentum is considered, it is necessary to use Transverse Momentum Dependent PDFs (TMD-PDFs). Eight TMD-PDFs are required to describe all the allowed correlations between the parent hadron spin, parton spin and parton transverse momentum at leading order. All of these functions are listed in figure 1.4 [10, 13].

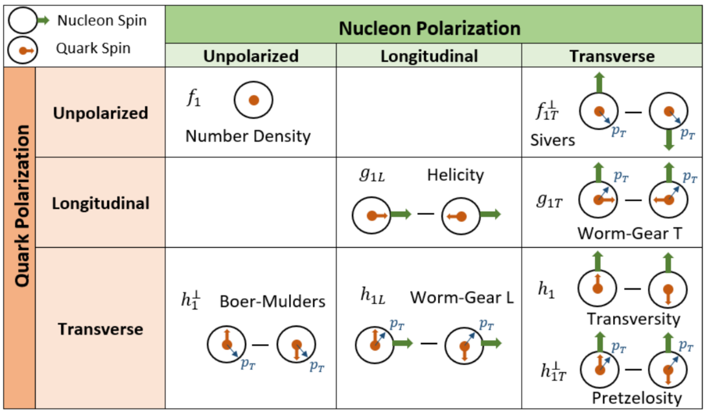

| Nucleon Spin<br>Quark Spin | | Nucleon Polarization | | |
|---|---|---|---|---|
| | | Unpolarized | Longitudinal | Transverse |
| Quark Polarization | Unpolarized | $f_1$ Number Density | | $f_{1T}^{\perp}$ Sivers |
| | Longitudinal | | $g_{1L}$ Helicity | $g_{1T}$ Worm-Gear T |
| | Transverse | $h_1^{\perp}$ Boer-Mulders | $h_{1L}$ Worm-Gear L | $h_1$ Transversity<br>$h_{1T}^{\perp}$ Pretzelosity |

Figure 1.4: The eight leading order TMD-PDFs in terms of the quark and of the nucleon polarisations [10]

All of the TMD-PDFs can be measured by SIDIS because the structure functions defined in 1.9 are convolutions of TMD-PDFs and TMD-FFs, the transverse momentum dependent fragmentation functions. In addition, the transversity PDF, the only collinear PDF that cannot be measured in DIS, can also be determined. So far, only the Sivers TMD is measured clearly non-zero. It is particularly interesting since it describes the correlation between nucleon spin and the transverse momentum of partons.

Figure 1.5 shows the transversity function extracted from the Collins asymmetry.

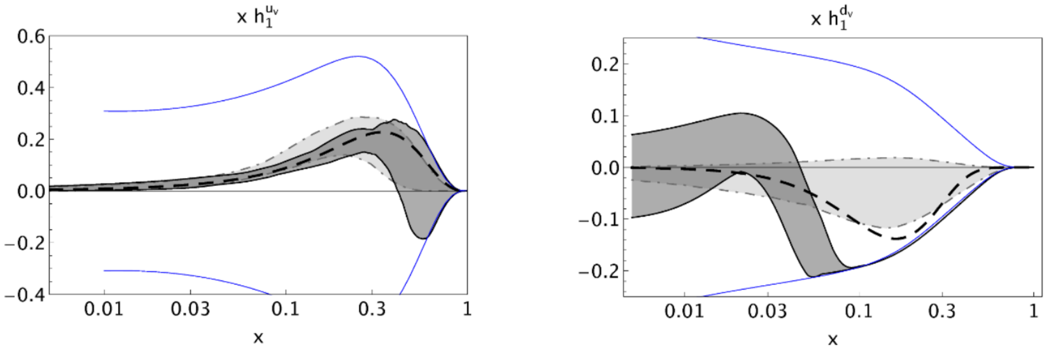

Figure 1.5: u and d quark transversity function extracted from Collins asymmetry [14]

Sivers function is presented in figure 1.6.

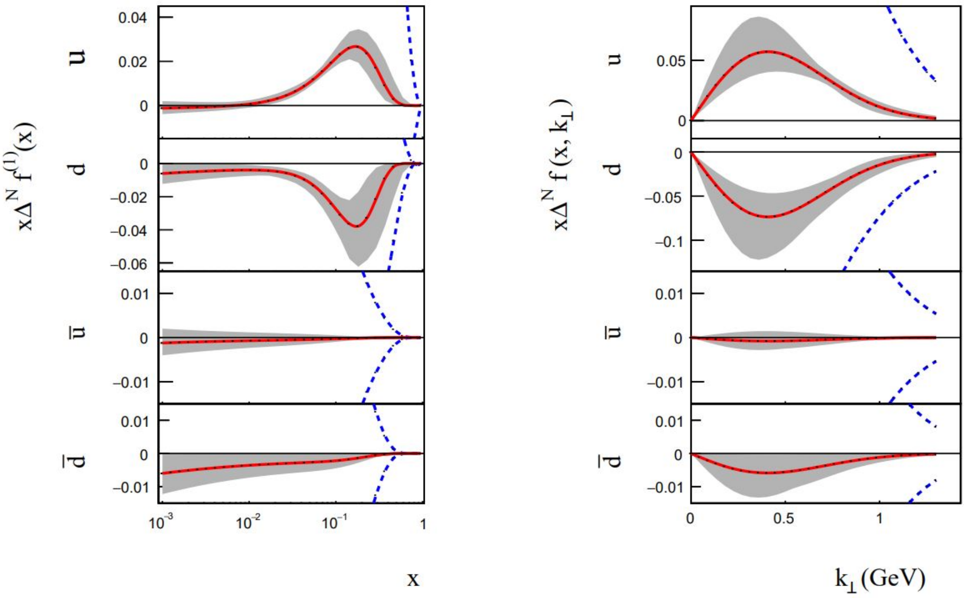

Figure 1.6: The first moment of the Sivers function extracted from the available SIDIS data, grey bands correspond to 90% confidence level [15]

# 2. COMPASS experiment

COMPASS (COmmon Muon Proton Apparatus for Structure and Spectroscopy) is a high-energy particle physics experiment at CERN's Super Proton Synchrotron (SPS). Its primary aim is to study the structure of hadrons and discover more about their property spin and its relation to the motion of quarks and gluons composing the particle [16, 17, 18].

It consists of many detectors that will be discussed in the following chapters. In figure 2.1, you can see the layout of the spectrometer from the top.

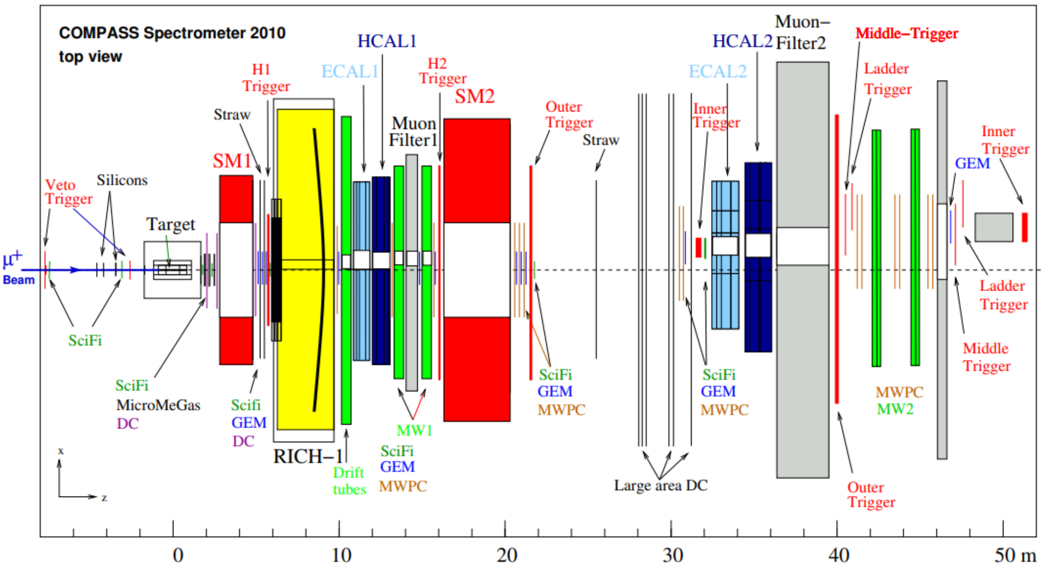

Figure 2.1: Top view of COMPASS experiment from 2010 [17]

## 2.1 Beam line

As previously mentioned, COMPASS is located at the CERN's SPS M2 beam line. The beam of protons accelerated by the SPS is extracted, and depending on the used target, there are three modes in which the M2 beam line operates [16, 18]:

1. High-intensity positive muon beam generated by the 400 GeV/$c$ SPS proton beam going through a 500 mm Beryllium target. It is obtained thanks to the weak decay of pions in the hadron beam and using absorbers to stop the remaining hadrons. The delivered muons have momentum between 60 to 190 GeV/$c$.

2. High-intensity hadron beam with momentum up to 280 GeV/$c$. This mode is set off by moving hadron absorbers from the path of the beam [16].

3. Low-energy low-intensity 40 GeV/$c$ electron beam for testing and calibration purposes [16].

## 2.2 Polarised target

A polarised target is used in particle physics experiments to measure the spin-dependent properties of subatomic particles. The cross-sections of two distinct spin configurations differ, and the COMPASS muon programme aims to measure these asymmetries. In order to determine them, the target needs to have a high degree of polarisation. This means the target nucleons need spin aligned in a specific direction. It consists of three cells, one central cell and two external ones, called upstream and downstream, based on the beam particle's direction of flight. The central cell is polarised in the opposite direction with respect to the other cells and is twice as long. The diameter of the target is 30 mm, the external cells are approximately 30 cm long, and the central one is 60 cm long. There is a 10 cm gap between the external and central cells [16].

Electron spins can be aligned using low enough temperatures and a strong magnetic field, but this is not the case for the nucleons, where only a tiny fraction can be aligned using magnets. This is why a microwave cavity is also a part of the polarised target, to enhance further the polarisation using dynamic nuclear polarisation (DNP), which transfers the electron polarisation to the nucleons using a microwave field [11, 16].

The dilution refrigerator (DR) is used to cool down the target material to about 60 mK to maintain a high degree of polarisation after the microwave field is switched off. It also allows the rotation of the spins from the direction parallel to the beam, where DNP operates, to the transverse direction. Figure 2.2 shows the scheme of the DR. However, it is important to point out that in 2022 data taking three cells were used compared to two cells in the picture.

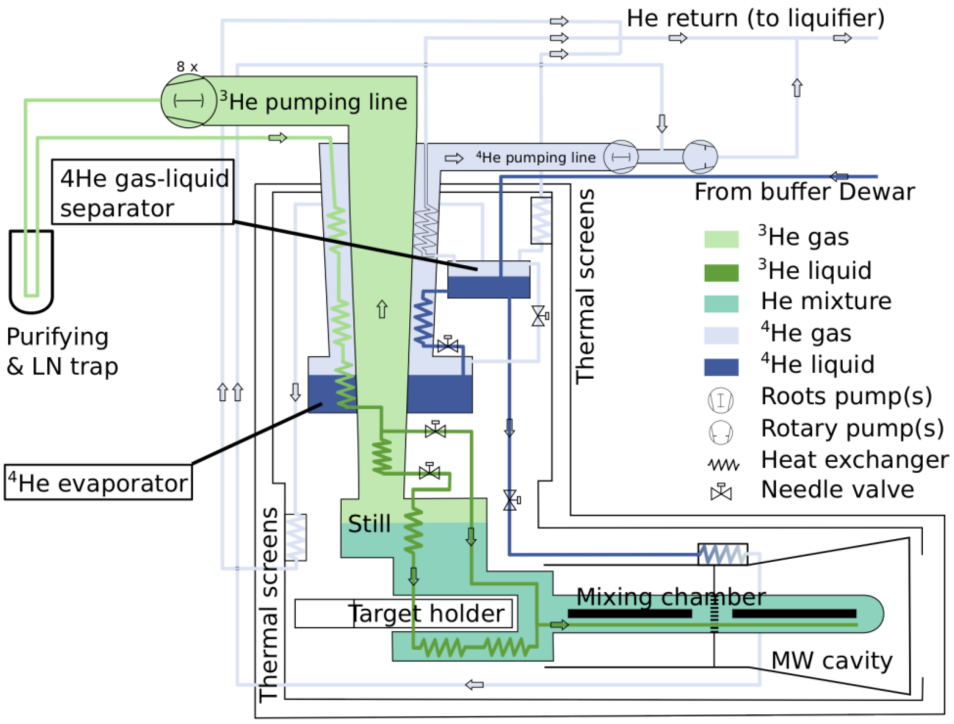

Figure 2.2: The scheme of the dilution refrigerator, picture by COMPASS collaboration

## 2.3 Tracking detectors

A significant part of COMPASS is the tracking system. It is distributed over the entire length of the spectrometer, and it consists of several types of detectors, where the detectors of the same type are approximately at the same z-coordinate, forming a tracking station [16].

Trackers are divided into three categories. The first category is very small area trackers (VSAT), which cover the area of the highest beam flux. That is a circle with a diameter of about 2.5 to 3 cm. The small area of the detectors and the high beam rate demands them to be extremely precise regarding the position or time measurement. At COMPASS, detectors like scintillating fibres and silicon microstrip detectors are used in these areas [16].

The next category is small area trackers (SAT), which cover a radial distance between 2.5 and 30 to 40 cm. Micropattern gas detectors such as micromegas and GEM detectors are employed for this task [16].

The last category is large area trackers (LAT). These trackers cover the areas furthest from the beam and consist mainly of drift chambers, straw tube chambers and multiwire proportional counters [16].

## 2.4 Particle identification

Several detectors ensure the proper identification of particles, including Ring Imaging Cherenkov (RICH), muon walls and calorimeters [16].

### 2.4.1 RICH

RICH is based on the effect of Cherenkov radiation. On account of this phenomenon, high-energy particles passing through the detector emit photons at an angle $\theta$ determined by the equation [6]

$$\cos\theta = \frac{c}{n v_p} \tag{2.1}$$

where $c$ is the speed of light, $v_p$ is the particle velocity, and $n$ is the refractive index of the medium, which is, in this case, $C_4F_{10}$ gas. Through this mathematical formula, the particle's speed can be determined, which, when compared to the particle's momentum measured in the spectrometer, allows the separation of passing hadrons into protons, pions, and kaons up to momenta of about 43 GeV/$c$ [6, 16].

### 2.4.2 Muon filters

Two muon filters detect scattered muons. Both consist of two parts: a hadron absorber and a tracking station, which is called a muon wall. The absorbers ensure that none of the hadrons passes through and prevent false particle identification. The first muon filter is a 60 cm thick iron plate, and a 2.4 m concrete block is used for the second one. The first muon wall (MW1) comprises two stations of squared drift tubes that provide an active area of 4.8 x 4.1 m$^2$. Each station has an average tracking efficiency of approximately 91%. The second muon wall is also constituted of two tracking stations, in this case, steel drift tubes, and has an active area of 4.5 x 2 $m^2$. Each station has an efficiency of about 82 % [6, 16].

### 2.4.3 Calorimeters

COMPASS includes two hadron calorimeters (HCAL) prior to the muon walls. They aim to measure the energy of the hadrons generated in the target and trigger inelastic muon scattering events. Both belong in the sampling calorimeters category, meaning they consist of two repeating constituents. The first is an iron plate, where the hadron showers are generated, and the second one is scintillator plates, which serve the purpose of measuring energy [16].

Electromagnetic calorimeters (ECAL) measure the energy of electrons and gamma rays, which develop an electromagnetic shower in the calorimeters and are entirely absorbed [6, 16].

## 2.5 Trigger

The trigger system is responsible for selecting the events of interest and reducing the produced data size to a manageable level. It operates in a very high-rate environment with a decision time below 500 ns and minimum dead time, in which it has to provide a read-out signal for the front-end electronics [16].

The trigger system contains four pairs of scintillating hodoscope stations, which are called the ladder (LT), the middle (MT), the outer trigger (OT) and the Large Angle Spectrometer Trigger (LAST). Another significant part of the trigger system is two scintillating veto stations upstream of the target and the hadron calorimeters [6, 16].

## 2.6 Data acquisition

COMPASS data taking is organised in runs, a collection of a maximum number of 200 spills. Spills refer to a 5s period in which the high flux of muons, about $2.8 \cdot 10^8 \mu$, is delivered to the target. Data taking is further divided into periods that usually last two weeks. The change of the polarisation of the target is done in the middle of the period. The Data Acquisition system (DAQ) is responsible for collecting the data selected by the triggers and creating the corresponding event [6, 16, 11].

## 2.7 Detector control and monitoring

The Detector Control System (DCS) is designed to record all the vital information about detectors, including voltages, temperature, gas pressures and much more. It also allows changing detector parameters remotely without the need to access the experiment hall [16].

Monitoring is done via DAQ, which allows users to observe various factors like beam characteristics, trigger rates and performance of the front-end electronics [16].

## 2.8 Event reconstruction

Event reconstruction is a crucial part of data analysis. The goal is to reconstruct particle properties for each collision fully. Measured data from all detectors are processed by a software package called CORAL. Input for the reconstruction includes the recorded data together with the Monte Carlo simulated data, the so-called alignment file, where the position of each detector is specified, and detector calibration [16, 19].

The reconstruction has many steps, including beam reconstruction, muon identification, track/particle association and much more. The complicated process is in figure 2.3. After it is finished, the reconstructed information is stored in ROOT ([20]) TTree files called mini Data Summary Tapes (mDST), which serve as an input for all following physics analyses [16].

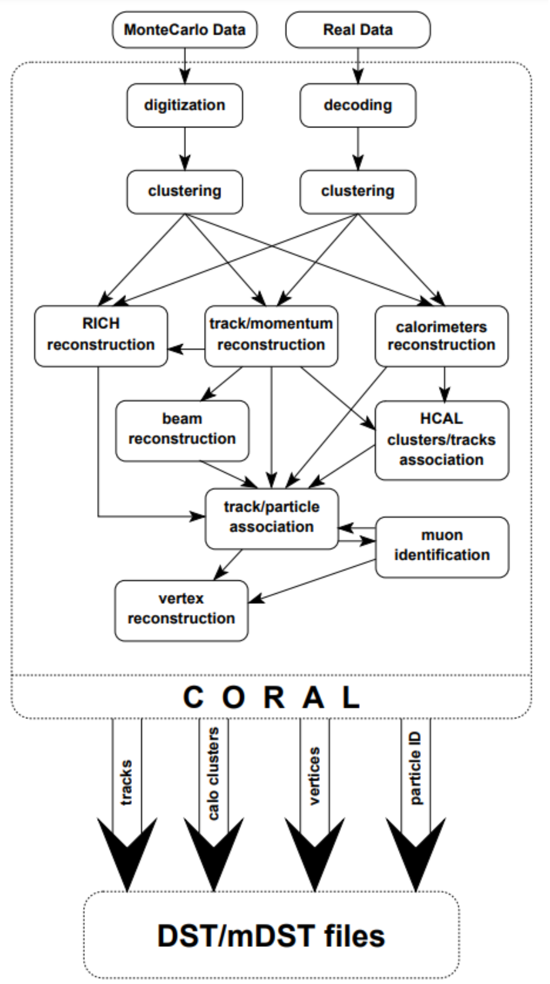

Figure 2.3: Scheme of event reconstruction [16]

The PHAST [21] (PHysics Analysis Software Tools) is a code developed for analysis. It provides a set of algorithms to compute physical variables and allows users to utilise many classes to process the reconstructed mDST files. For all further analysis, the PHAST was used.

# 3. Polarised target analysis

The analysis of the polarised target was done to check whether the distribution of vertices and beam tracks is uniform, to compare them in different parts of the target and to study the density of the target. The target axis coordinates, and cell boundaries were found by analysing the created plots. The data from period W07t2 were used for this analysis.

## 3.1 Vertices

The first step was to create histograms of vertices. Vertices meaning the points at which the beam particles interact in the target material. The following cuts were used for event selection:

- Only physical triggers (MT, LT, OT and LAST)
- There is an incoming particle
- There is an outgoing scattered $\mu$ (checked by iMuPrim(0, 1, 1, 0) function)
- $0.1 < y < 0.9$
- $Q^2 > 0.8$

$X$ and $Y$ projections of all vertices are shown in figure 3.3. The number of vertices is proportional to the density of the target material and to the beam intensity at the given point in space. Because the target is circular, its midpoint is located at the origin of the coordinate system and the beam intensity has a roughly Gaussian shape centred on the target, the plots meet the expectations, as the distributions peak by the middle of the target in both cases.

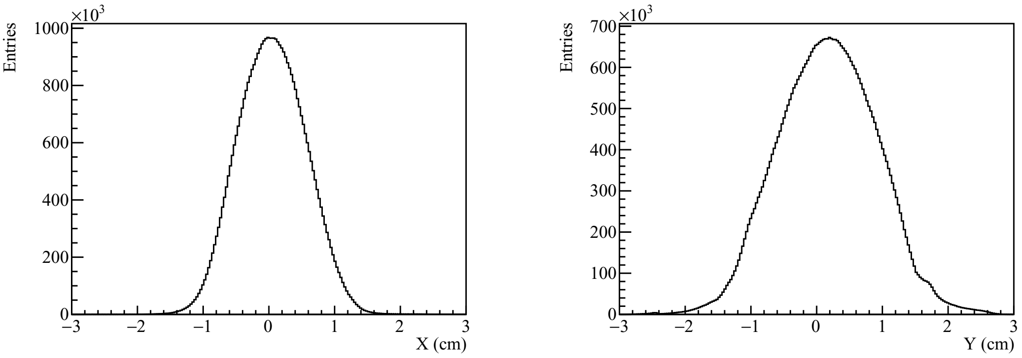

Figure 3.1: $X$ and $Y$ projections of vertices

A two-dimensional histogram of all vertices projected on the $XY$-plane is pictured in figure 3.2, where the white dotted circle represents the target's position. The process of finding the target's coordinates is described at the end of this chapter, together with the process of finding the cell boundaries.

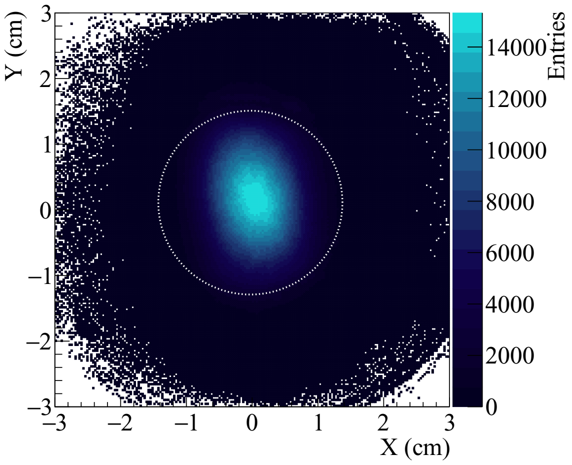

Figure 3.2: Two-dimensional histogram of all vertices in target

Figure 3.3 illustrates the distribution of vertices over the $Z$-axis. The vertical lines represent the boundaries of the three target cells. Based on the expectations, the number of entries should be constant in each one of the cells and should strongly decrease in the gaps between them because, as was already noted, the number of vertices is dependent on the density of the material. This is true for most parts of the graph. Although there are some exceptions, like the upstream end of the central cell, where a more rapid increase of entries was expected. This means that this part of the cell contains less material than the rest.

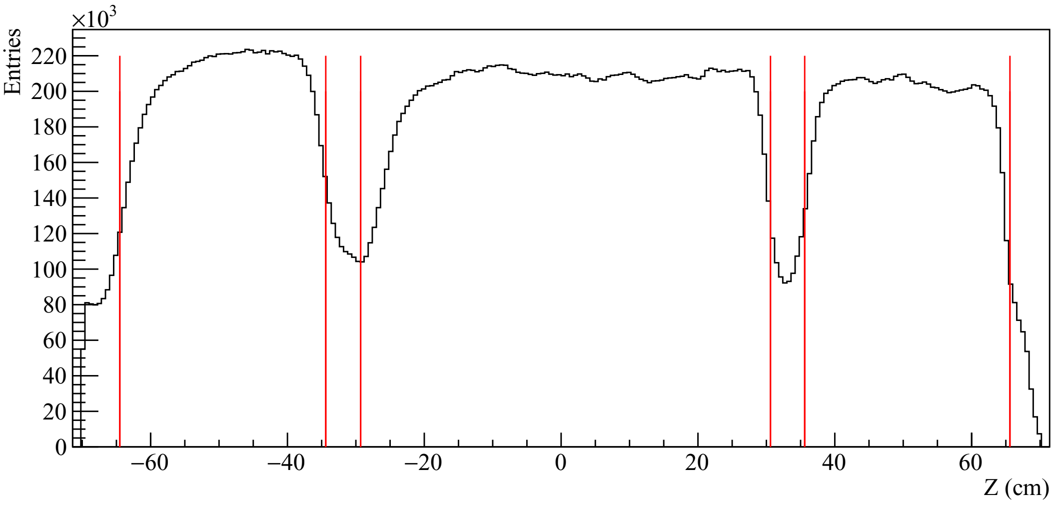

Figure 3.3: $Z$ projection of vertices

To further smooth out the dependence in the region of the cells, a radial cut $R < 14$ mm eliminating all vertices outside the target, which contained contribution from holding structures, cables and polarisation-measuring coils, was implemented. Figure 3.4 shows all vertices distribution after the radial cut.

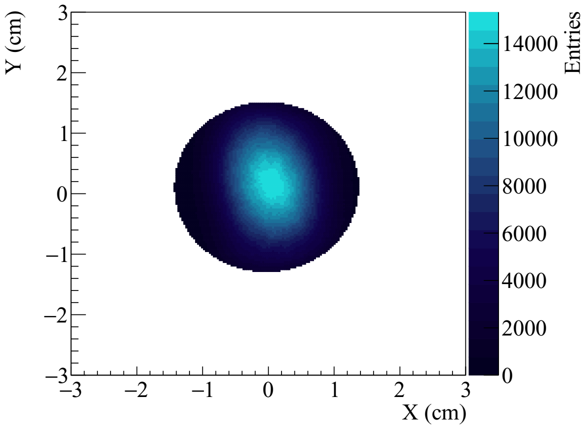

Figure 3.4: Projection of all vertices in target on the $XY$ plane

All of these vertices were again projected on the $Z$-axis. The result of this process is pictured in figure 3.5. Comparing this plot with 3.3, it is clear that the radial cut cleared out some of the inconsistencies, especially in the middle and downstream target cell.

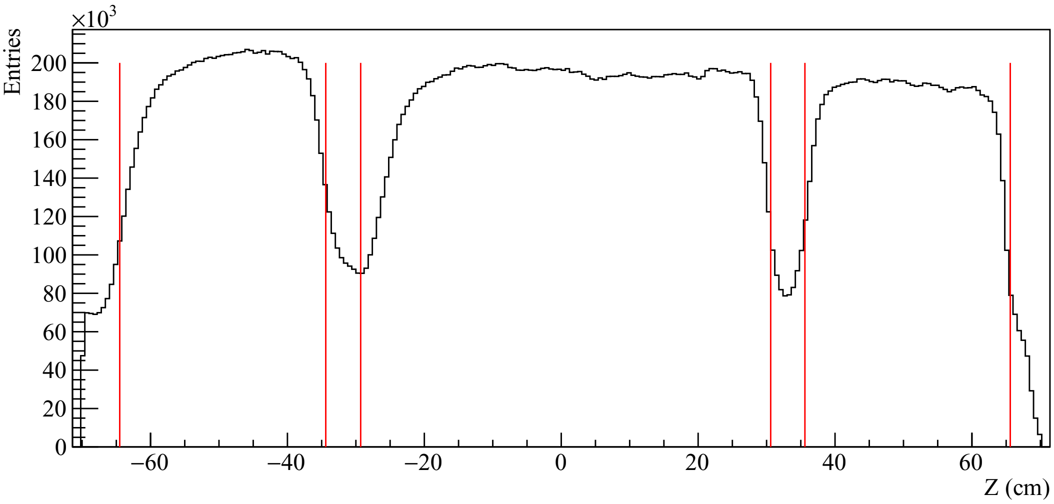

Figure 3.5: $Z$ projection of vertices after the radial cut $R < 14$ mm

All of the vertices were also projected on the $XZ$ and $YZ$ planes. Figure 3.6 shows resulting histograms, where the white dotted rectangles represent the target cells. It is again visible that there is a smaller amount of vertices in the upstream end of the central cell, particularly in the $YZ$ plane.

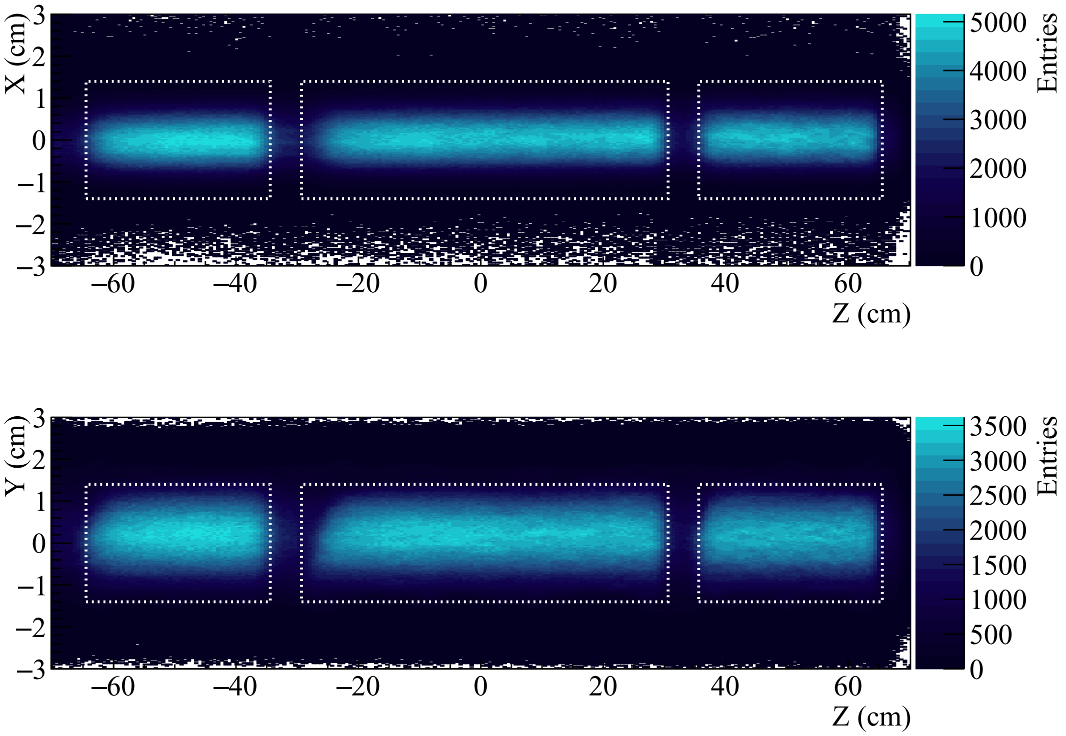

Figure 3.6: Projection of vertices on the $XZ$ and $YZ$ plane

## 3.2 Beam tracks

The beam tracks refer to tracks of the particles incoming from the M2 beam line, which were detected before they hit the target. The suitable beam tracks were selected by the following cuts:

- Only random trigger (TRand)
- It is a beam particle (checked by IsBeam() function)

Similarly, as in the case of vertices, two histograms were created (figure 3.7) to picture the distribution of beam tracks on the $X$ and $Y$ axis. These histograms are very similar to histograms of projected vertices 3.3.

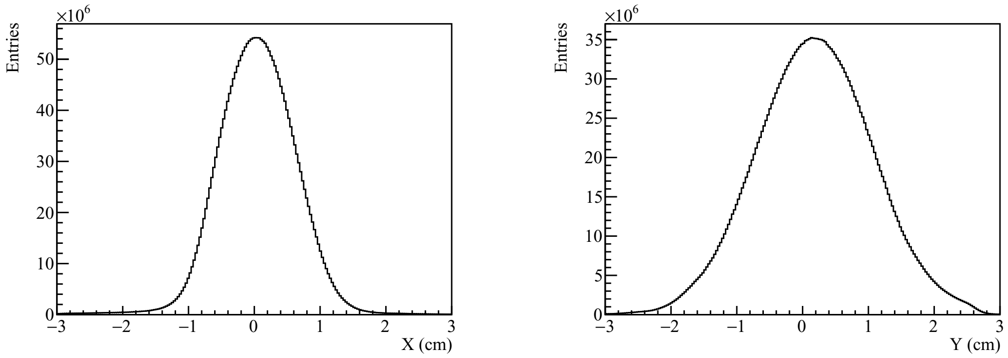

Figure 3.7: $X$ and $Y$ projections of beam tracks

Figure 3.8 illustrates a two-dimensional distribution of beam tracks; the dotted circle represents the target.

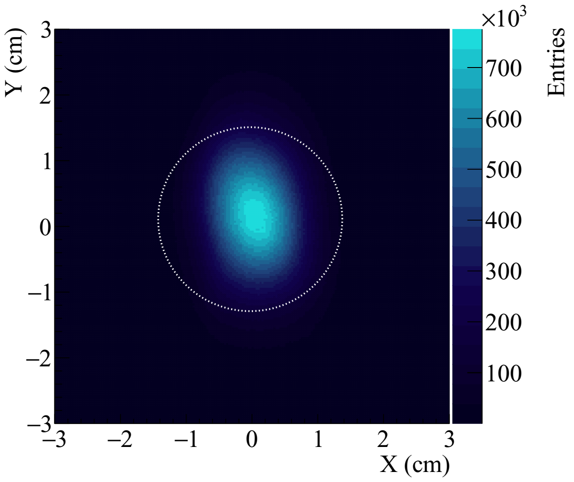

Figure 3.8: Two-dimensional beam track distribution projected to $XY$ plane

## 3.3 Target density

Using the distributions of beam tracks and vertices, it is possible to use relation 3.1 to determine the dimensionless target density by dividing the histogram of vertices by the histogram of extrapolated beam tracks.

$$\rho_{target} \sim \frac{N_{vertices}}{N_{beamtracks}}. \tag{3.1}$$

Figure 3.9 displays the result for all the vertices and beam tracks. The expectation matches the result, a homogeneous density in the area of target cells and a sudden decrease outside of it.

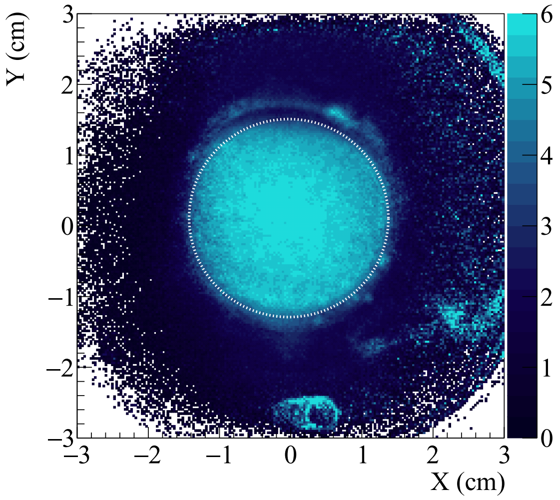

Figure 3.9: Target density

The target density was also pictured for four different intervals to see the dependence on the $Z$ coordinate. For each of the four intervals, only vertices in the specified range were used, and the same goes for the beam tracks, which were extrapolated to each corresponding bin in the $Z$ axis.

Interestingly, it turns out that the shape in the lower part of figure 3.9 is actually a circle in the four following plots 3.10. This means that this region of higher density is caused by the $^3$He distribution pipe, which slightly changes its $X$ coordinate over the target, which results in an oval shape. Another regions of higher density around the target are probably caused by polarisation-measuring NMR coils, thermometers and their cabling.

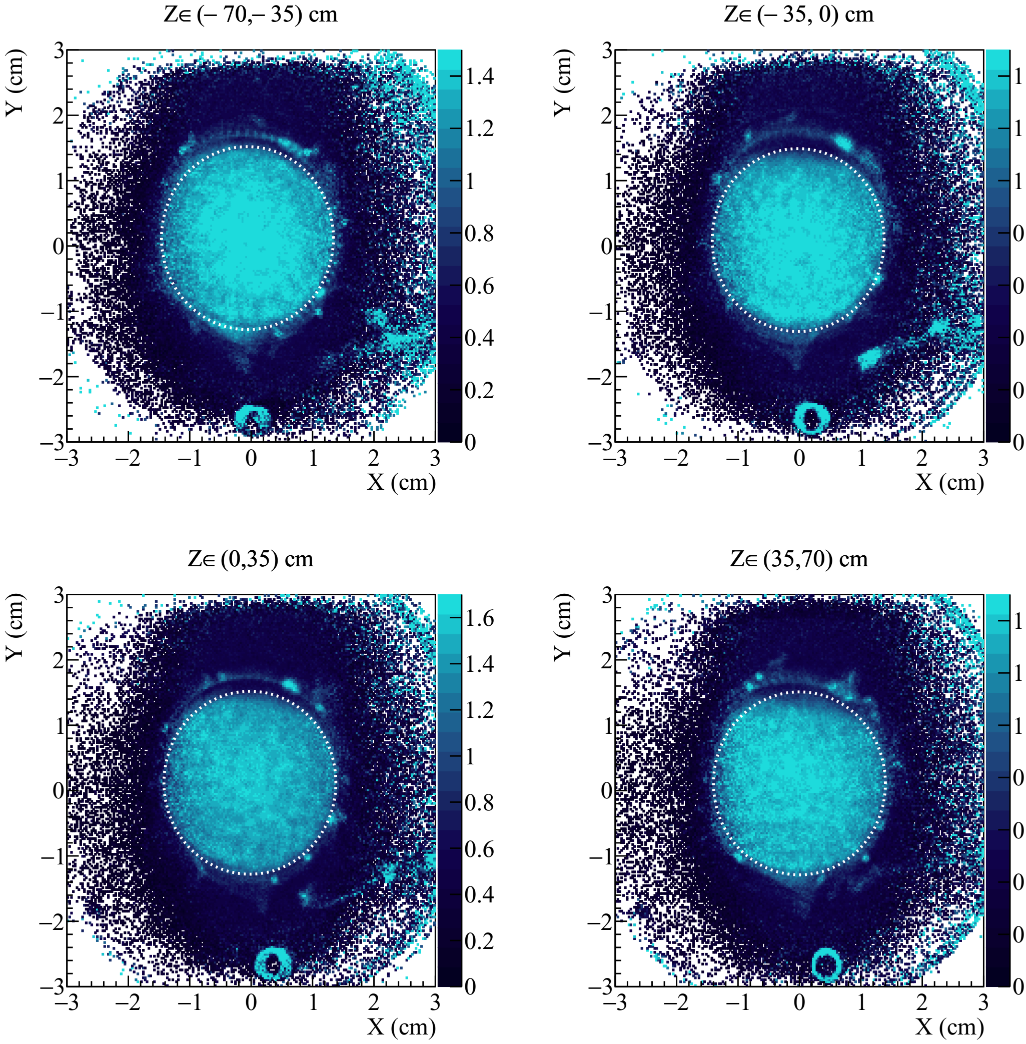

Figure 3.10: Target density in four intervals

Using the extrapolation of the beam tracks over the whole target, the density was also depicted in the $XZ$ and $YZ$ plane. Figure 3.11 shows resulting histograms.

What's interesting is that there is a stripe of higher density visible in the $XZ$ plane going through the whole target at approximately $X = 0$. This is again caused by the $^3$He distribution pipe going through the lower part of the target, as in the case of the $XY$ plots of densities.

There is also an unexpected density drop by the central cell's upstream end. It is for the same reason as in the case of the vertices plot 3.6. This part of the cell contains less material than the rest. Apparently, the cell was not fully filled with material beads. The shape of the empty region comes from the filling procedure, during which the target is inclined.

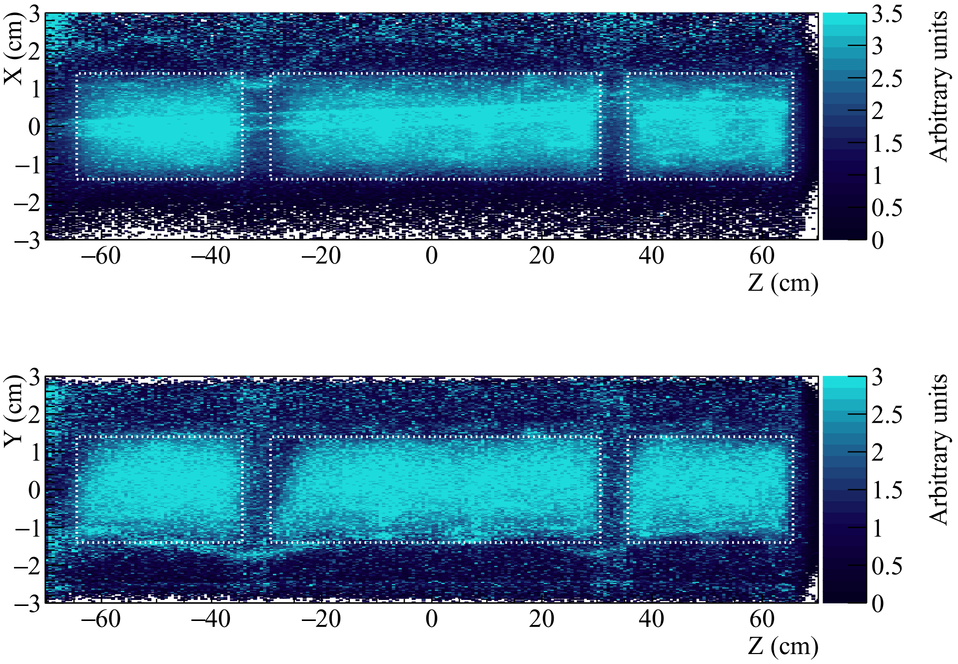

Figure 3.11: Target density from side view

The generated histograms of the target density were compared to photos of the target holder, which are presented in figures 3.12 and 3.13. Several components of the target that are suspected to cause regions of higher density are visible in the pictures, such as the helium pipe in figure 3.12 (b). Other visible components are cables.

(a) (b)

Figure 3.12: Photos of the polarised target holder, picture (a) shows the full target holder including the cables, and picture (b) shows the cross-section of the target holder with the $^3$He pipe visible in the upper left part

Figure 3.13: Full view of the target holder

## 3.4 Target position

All four histograms in figure 3.9 were used to find the target's position. A circle with a target radius ($r = 1.4$ cm) was fit by eye to match the area of homogeneous density for all of these plots. The coordinates of the circle's midpoints were displayed in two plots, the dependence of the $X$ coordinate on the $Z$ axis and the same dependence for the $Y$ coordinate. As the $Z$ coordinate, the middle of the corresponding interval was used. Figure 3.14 shows the found dependencies.

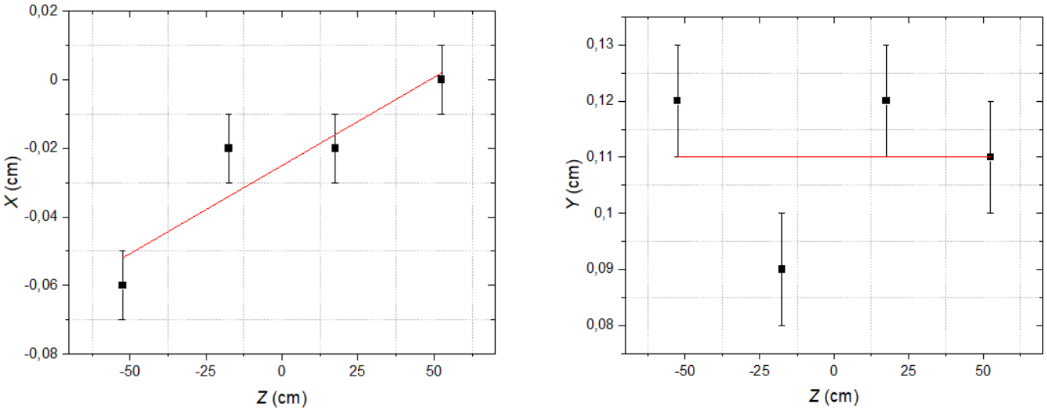

Figure 3.14: Linear fit of the circle's midpoints; 0.1 cm was used as the uncertainty of determining the exact position

Using the results of the linear fit, the midpoint of the target was determined to lie on an axis given by two points:

$$
\begin{aligned}
P_1 &= (-0.052, 0.11, -52.5)\ \text{cm} \\
P_2 &= (-0.002, 0.11, 52.5)\ \text{cm}
\end{aligned}
$$

For a specific $Z$ value, the Y coordinate of the target's midpoint remains the same. The X coordinate can be found utilising the equation

$$X = (-0.052 + \frac{0.05}{105} Z) \text{ cm}. \tag{3.2}$$

## 3.5 The position of the target cells

The side view of target density plots was used to find the position of the cells on the $Z$ axis. To get the best results, only the area of the target that does not have a problem with cell filling was used. This means that a significant part of the plot 3.11 had to be omitted to avoid the unsuitable upstream part of the central cell. The ranges of $X$ and $Y$ that were used are $X \in (-1, 1)$ cm and $Y \in (-1, -0.5)$ cm.

After the cut, the target density plot was projected on the $Z$ axis. The gap size and cell lengths were known, so only one $Z$ value had to be specified to find the cell coordinates. For this, the gap between the upstream and central cell was fitted by a parabola, and its minimum was used as a midpoint of the gap. The red parabola and red vertical lines in figure 3.15 show the results for this procedure. To make this more accurate, the same was done for the gap between the central and downstream cells; the results are, in this case, in blue colour.

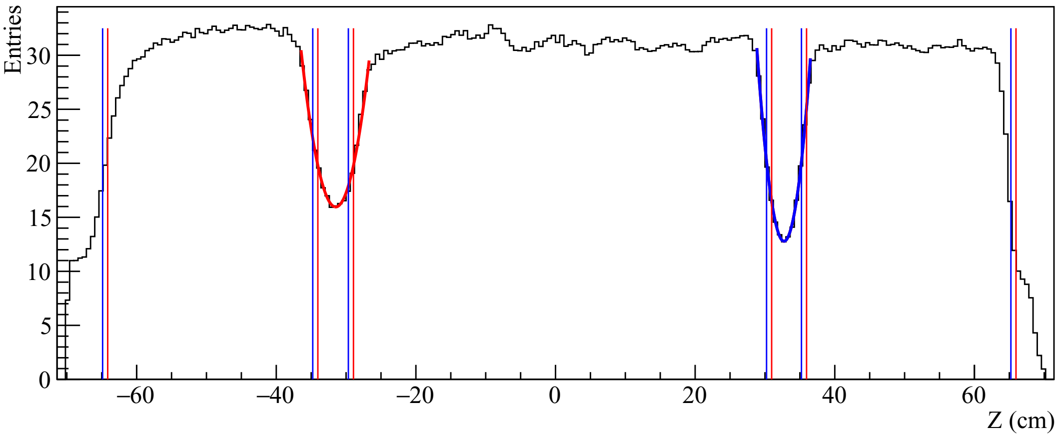

Figure 3.15: The density projection on the $Z$ axis for entries in $X \in (-1, 1)$ cm and $Y \in (-1, -0.5)$ cm

The final result was found by averaging the results. Here are the coordinates of all three cells:

$$\begin{aligned} \text{Upstream cell: } & (-64.5; -34.4) \text{ cm}, \\ \text{Central cell: } & (-29.3, 30.6) \text{ cm}, \\ \text{Downstream cell: } & (35.6, 65.6) \text{ cm}. \end{aligned}$$

## 3.6 Summary

**Target position**
The results suggest that the target axis is well-centred. The target cells are well aligned in the $Y$ coordinate and have only a slight slope in the $X$ coordinate. This is a good result considering the complex structure of the target.
**The position of the target cells**
The results obtained by fitting the two gaps between the cells are similar. Considering the values obtained from 2021 data, the fit of the first gap gives a cell position shifted by $+0.26$ cm. The fit of the second gap is shifted by $-0.47$ cm. The final values found by averaging consequences in a shift of $-0.11$ cm.

# 4. Bad spill analysis

The asymmetries extraction requires stable spectrometer acceptance over two subperiods of data taking. The stability is checked by the so-called bad spill and bad run analysis. The bad run analysis is not part of this work. Bad spill analysis consists of monitoring variables closely correlated to the detector's stability. The measured data should be constant if the detectors were stable during the data-taking period. The instability of the detectors will have an impact on the monitored variables, which causes an inconsistency in their values over time. This could produce problematic data, which would lead to false asymmetries. The goal of the analysis is to reject faulty sets of data [5].

An essential part of bad spill analysis is choosing the proper variables to monitor. As mentioned, the chosen variables must be closely correlated to detector stability. One of the most suitable ones are macro variables and inclusive trigger variables. Here is the complete list of variable classes checked during the first phase of bad spill analysis [5].

- Macro variables class
    - the number of beam particles per vertex
    - the number of tracks per primary vertex
    - the number of primary vertices per event
- Inclusive trigger class
    - the number of inclusive trigger per the number of beam particles (MT, LT, OT, CT)

The point of this first phase was to adopt the basic skills of finding the optimal options for rejecting bad spills. This topic will be closely discussed in the next section.

## 4.1 Selection of bad spills

The next step in bad spill analysis is finding suitable options to reject bad spills. To determine if a spill is good or bad, monitored variables of each spill are compared to the variables of neighbouring spills. This is done for a specific number of neighbours $N_n$, which is by default set to 600. Each spill is compared to, in total, 1200 other spills. Comparing is done in both directions, with 600 spills to the left and 600 to the right. For spills near the beginning or end of the period that do not have enough neighbours in one direction, the interval gets enlarged on the other side to ensure that each spill is compared to 1200 other spills. In some cases, it is better to change the interval length over which the variables are compared. This will be discussed in the text later [5].

This procedure assigns each spill a number of good neighbours $N_{gn}$. To decide if a spill is counted as a good neighbour, the values of the compared variables need to be within certain boundaries, which are given by multiples of the root mean square (RMS) of the distribution determined in a restricted region with no steps and large fluctuations, which would spoil up the RMS value. The RMS for a set of $N_n$ values is given by the equation

$$x_{RMS} = \sqrt{\frac{1}{N_n}\sum_{i=1}^{N_n}(x_i - \bar{x})^2}, \tag{4.1}$$

where the $\bar{x}$ is the mean over $N_n$ values

$$\bar{x} = \frac{1}{N_n}\sum_{i=1}^{N_n} x_i. \tag{4.2}$$

Now that the RMS value is found, the boundaries are given by $\sigma$ in the units of $x_{RMS}$, and it is usually set between three and five [5]. Each neighbouring spill with index $j$ is counted to the total number of good neighbours $N_{gn}$ of the spill $i$ if it satisfies the inequality

$$|x_i - x_j| < \sigma x_{RMS}, \tag{4.3}$$

where $x_i$ is the value of the compared variable for the spill with index $i$ and $x_j$ is the same for spill $j$.

Now that $N_{gn}$ is assigned to each spill for each $\sigma$, the results can be plotted in histograms. A histogram for every value of $\sigma$ between 2 and 13 is created for each class of monitored variables. Figure 4.1 depicts an example of good distribution of neighbours. There is a small peak by 0, caused by genuinely poor spills with a deficient number of good neighbours. On the other side of the graph, there is a significant peak consisting of good data sets, which have many good neighbours.

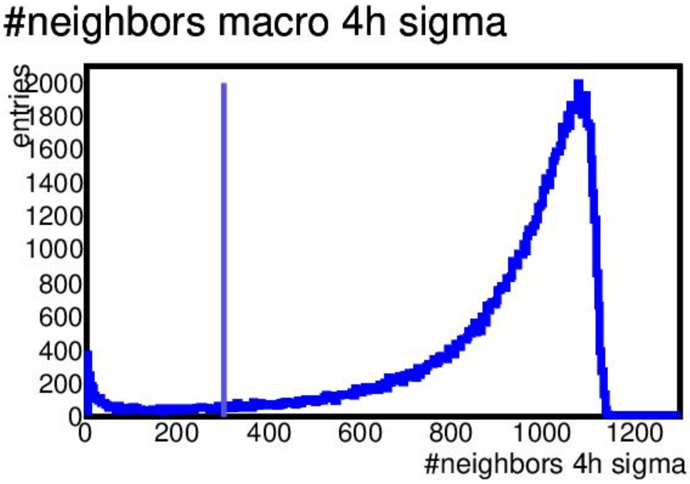

Figure 4.1: A good distribution of neighbours

To finally reject the bad spills, the number of required good neighbours $N_{req}$ is set. Spills with a lower amount of good neighbours are rejected. In the histogram 4.1, this value is set to 300 and is represented by a vertical line.

Two histograms of bad distribution of neighbours are depicted in figure **??**. In the first case 4.2, the $\sigma$ value is set too low, resulting in one merged peak. This distribution is too strict, which results in the rejection of many good spills. In contrast, in figure 4.3, the $\sigma$ value is set too high. This has the opposite effect. Very few spills are considered bad and rejected.

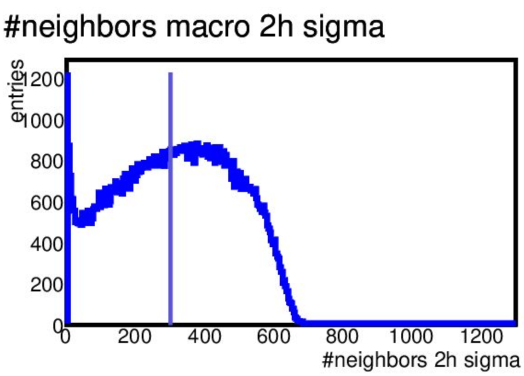

Figure 4.2: Sigma value set too low

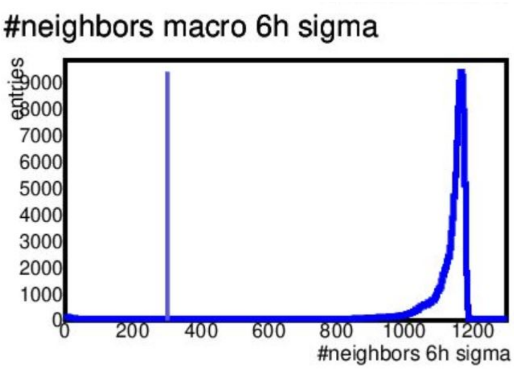

Figure 4.3: Sigma value set too high

To show how these inadequate $\sigma$ values affect the rejection of spills, examples of macro variables were plotted for both of these bad options. The results are in figure 4.4 and 4.5.

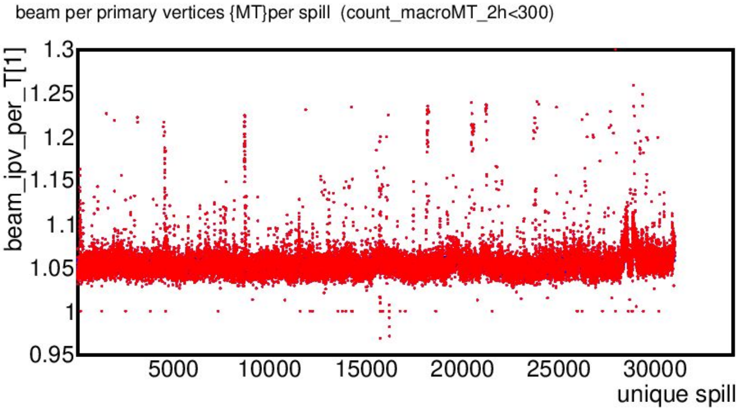

Figure 4.4: Resulting plot for $\sigma = 2$

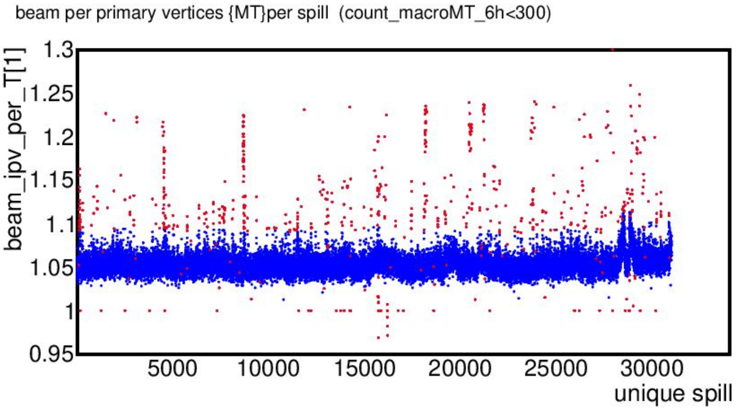

Figure 4.5: Resulting plot for $\sigma = 6$

The numbers of rejected spills and corresponding percentages are presented in table 4.1.

Table 4.1: The results of bad settings

| Options | #rejected spills | percentage |
|---|---|---|
| $\sigma$=2 | 18444 / 30991 | 59.5 % |
| $\sigma$=6 | 626 / 30991 | 2.0 % |

## 4.2 Removing islands of bad spills

Islands of bad spills refer to spills inconsistent with the rest of the measured data. Figure 4.6 shows an example of many islands in the W03t1 period. Most are small and easy to remove by adjusting the rejection parameters. The main problem is three bigger islands in intervals:

- (15 320 – 16 180)
- (20 810 – 21 376)
- (29 200 – 29 800)

The first two intervals are visible in the LAST per spill histogram and the third one in the OT per spill histogram. All of these spills are shifted towards lower or higher values, and they need to be rejected.

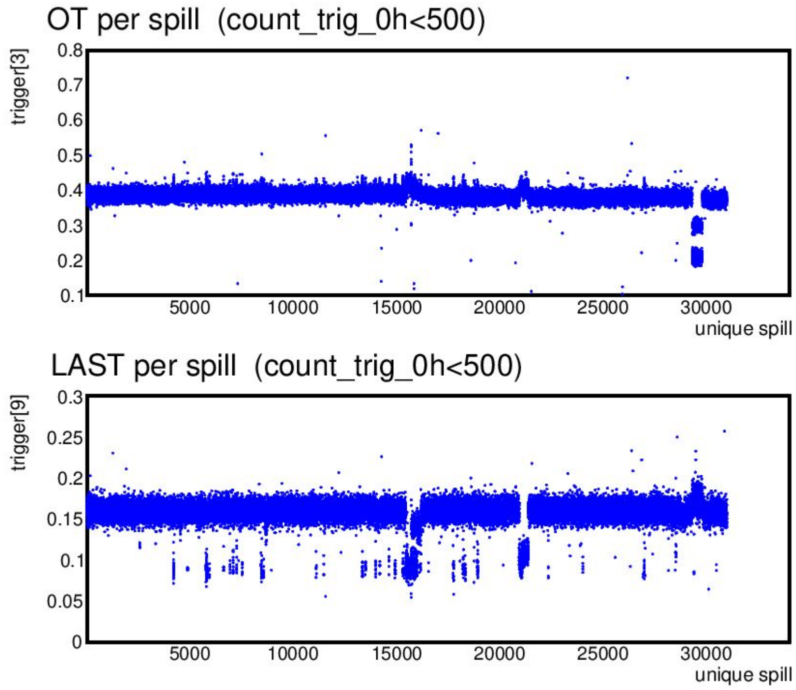

Figure 4.6: An example of distribution with bad spill islands

There are two strategies for removing bad spills. The first is to find the options strict enough to remove the islands entirely. The second method is to ignore the islands and add them to the final bad spill list manually. Both strategies are discussed in more detail later.

Later in the chapter, there are the full results for this period, where in the end, four bad spill islands had to be removed. Only three of them are discussed here for brevity. The fourth one is visible in the distribution of the number of beam tracks per the number of primary vertices, and its treatment is analogous to the first three.

### 4.2.1 Strict options

This method focuses on finding the number of neighbours $N_n$, over which the number of good neighbours is counted, the $\sigma$ value, and the number of required good neighbours $N_{req}$, that entirely remove islands of bad spills. The main disadvantage is that many good spills are also rejected with the islands of bad spills. The figures below illustrate an example of this strict cut.

Figure 4.7 shows the distribution of neighbours for the same plots as in figure 4.6. When using this strategy, it is essential to set the interval over which the good neighbours are calculated relatively high; otherwise, a spill in the island has enough compatible neighbours within the same island. It should be comparable or even higher to the number of spills forming the islands. In this case, the interval length was kept at six hundred, as the islands are approximately the same size. The next step is to eliminate the island by setting the required number of good neighbours. In this case, it was set to 500 for $\sigma$=4. It is often not obvious how to find the correct settings. The selection criteria are iteratively changed by inspecting the relevant distribution.

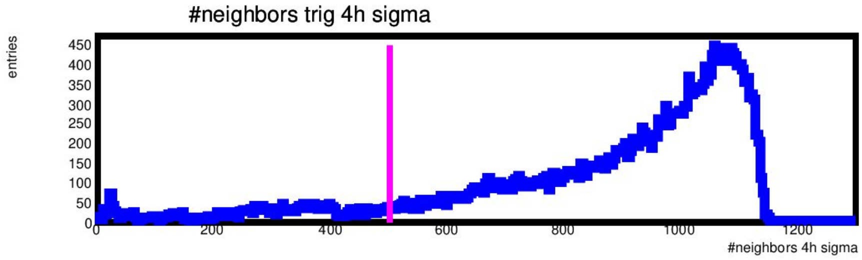

Figure 4.7: Histogram of good neighbours

Figure 4.8 shows two distributions of rejected spills with the final criteria applied for the trigger.

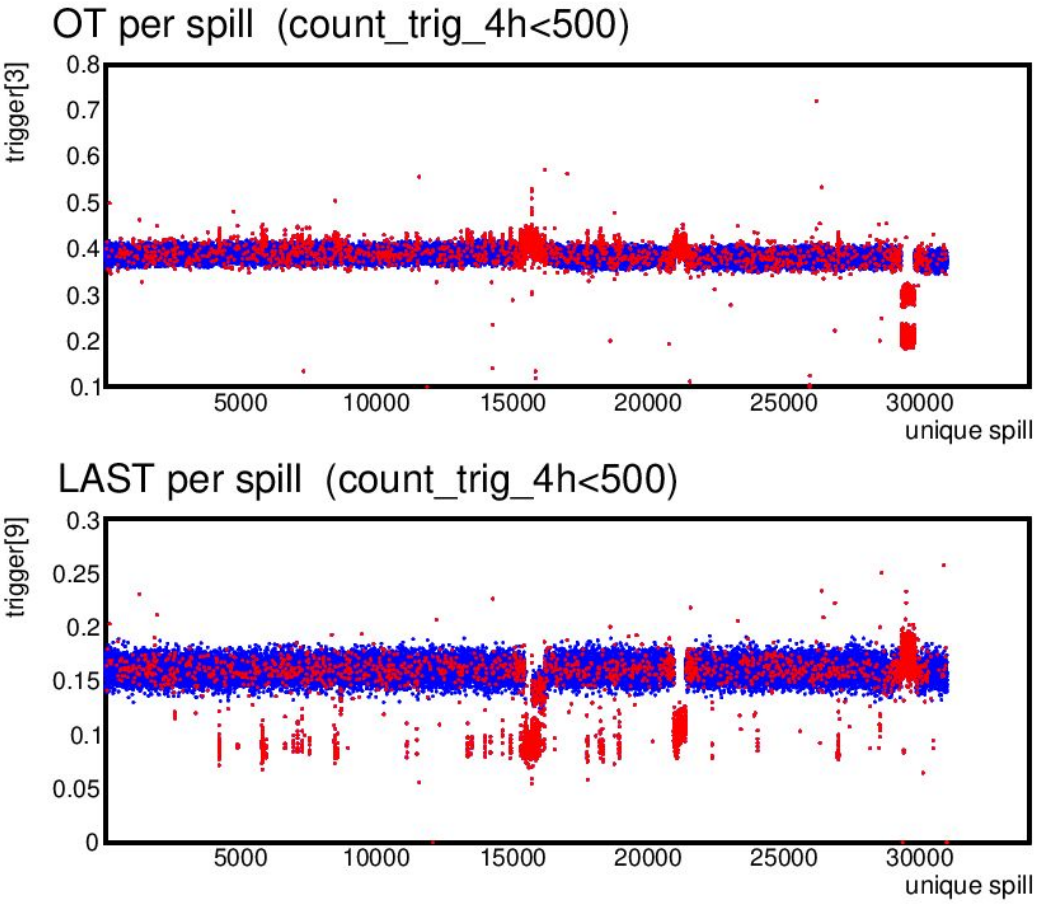

Figure 4.8: Final cut for strict options

### 4.2.2 Manual rejection

The other option is to reject bad spills manually. Using this method, the set options can be much less strict, and the final number of rejected spills is much lower. Figure 4.9 shows the distribution of neighbours with the cut.

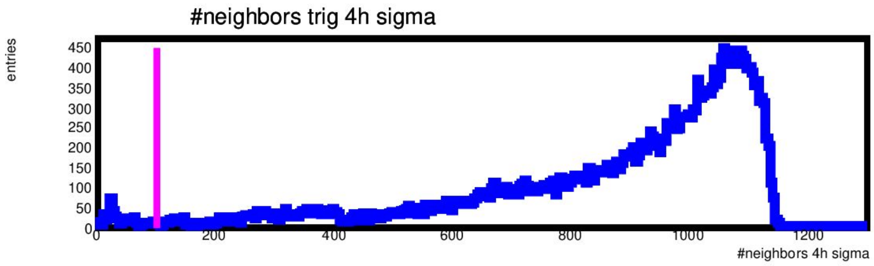

Figure 4.9: Distribution of neighbours for the manual rejection

Figure 4.10 illustrates the final plot of rejected spills. It should be pointed out that most of the spills comprising the islands are marked as good.

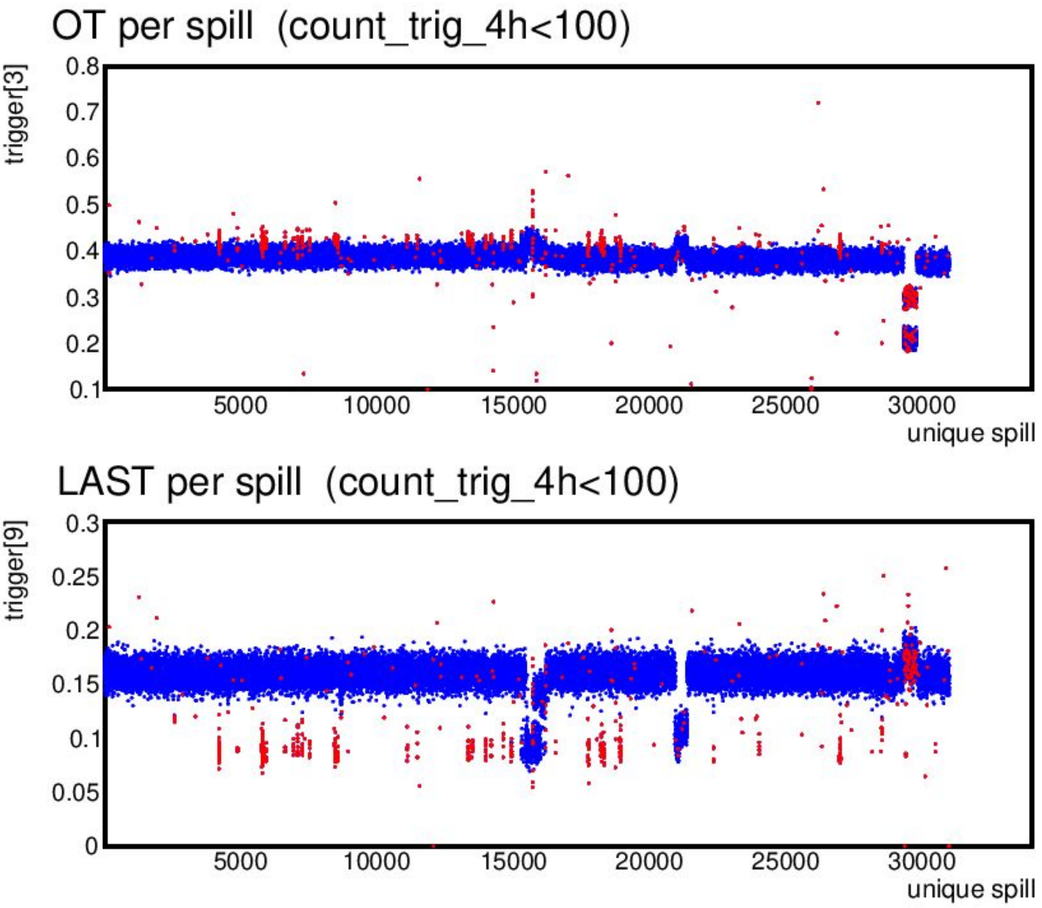

Figure 4.10: Final cut for manual rejection

In order to apply the manual rejection of the islands, it is essential to find out to which run the bad spills belong. For this, the *unique spill* number of the spills on the $X$ axis in figure 4.10. This number can be determined from the generated plots.

Now that the *unique spill* number is specified, it is possible to identify to which run these spills belong. In the text file generated together with the graphs named *badspill_q2_all_list_details.txt*, there are three columns of values. The first column contains the run number, the second column the number of rejected spill in the run and the third column the *unique spill* number. After finding the *unique spill* number, the run is identified and can be added to the final list of bad runs.

The details about the runs comprising the islands can also be found in the COMPASS logbook. Often these runs were marked as problematic already by the shift crew during the data taking.

## 4.3 Analysis of W03t1

The first data-taking period that was analysed is W03t1. Table 4.2 shows optimised selection criteria.

Table 4.2: Options for W03t1

| Class | $\sigma$ | $N_{req}$ |
|---|---|---|
| macro | 4 | 150 |
| MT | 4 | 160 |
| LT | 4 | 160 |
| OT | 4 | 130 |
| LAST | 4 | 160 |
| trigger | 4 | 100 |

Table 4.3 shows the spill rejection results based on the above criteria. These numbers do not include the number of manually rejected spills.

Table 4.3: Statistics of W03t1

| Class | Rejected spills | #Rejected spills out of 30991 |
|---|---|---|
| macro | 3.09% | 958 |
| MT | 3.03% | 938 |
| LT | 2.36% | 730 |
| OT | 2.85% | 882 |
| LAST | 2.96% | 915 |
| trigger | 2.00% | 621 |
| Total | 6.77% | 2099 |

After investigating the generated plots, in total, four islands of bad spills had to be rejected. The corresponding runs were found for each of these *unique spill* intervals and were checked in the COMPASS logbook. Table 4.4 illustrates the detector problems corresponding to the islands; the PMM abbreviation stands for pixel MicroMega, PGEM for pixel Gas Electron Multiplier and MA01Y1 and MA02Y1 denote part of the MW1 plane.

Table 4.4: Run problems W03t1

| *unique spill* | Run | Problem |
|---|---|---|
| 15 320 – 16 180 | 295 750 – 295 774 | MW1 errors |
| 19 000 – 19 960 | 295 837 – 295 848 | MW1, PMM and PGEM errors |
| 20 810 – 21 376 | 295 859 – 295 866 | MW1, MA01Y1-Y4, MA02Y1-Y4 |
| 29 200 – 29 800 | 295 956 – 295 966 | Unstable beam, MW1 and MW2 errors |

In total, 4683 spills out of 30 991 were removed by the algorithm and the manual island rejection, corresponding to 15.11% of rejected spills. This period was also analysed with the strict method, which resulted in slightly worse results; the percentage of rejected spills was 16.66%.

## 4.4 Analysis of W07t2

The second analysed period is W07t2, collected in the later part of the 2022 run and according to the logbook, it was more stable. Also, the reconstruction of this period is already the second iteration, and thus it is more refined. Table 4.5 shows options modified for this period.

Table 4.5: Options for W07t2

| Class | $\sigma$ | $N_{req}$ |
|---|---|---|
| macro | 3 | 70 |
| MT | 4 | 100 |
| LT | 3 | 100 |
| OT | 4 | 60 |
| LAST | 4 | 120 |
| trigger | 5 | 100 |

Table 4.6 comprises values obtained by applying these settings.

Table 4.6: Statistics of W07t2

| Cut | Rejected spills | #Rejected spills out of 39 443 |
|---|---|---|
| macro | 3.78% | 1490 |
| MT | 3.17% | 1250 |
| LT | 4.47% | 1763 |
| OT | 3.08% | 1213 |
| LAST | 2.66% | 1049 |
| trigger | 1.07% | 424 |
| Total | 6.39% | 2521 |

As in the case of W03t1, the manual rejection method was used. After assigning the run numbers to these intervals, the runs were again checked in the COMPASS logbook. The detector problems corresponding to the islands are in table 4.7.

Table 4.7: Run problems W07t2

| *unique spill* | Run | Problem |
|---|---|---|
| 5 895 – 6 500 | 297 279 – 297 282 | PMM errors |
| 9 630 – 9 840 | 297 303 – 297 304 | no MW2, part without beam |
| 10 585 – 10 920 | 297 308 – 297 311 | MW1, MW2 errors |

Adding the number of manually rejected spills to the statistics results in 3 426 / 39 442 rejected spills, which accounts for 8.69%. This is a much better outcome than in the case of W03t1, as was expected.

## 4.5 Evaluation of the impact of bad spills rejection

Three runs from the W07t2 data-taking period were randomly chosen to check the effect of the bad spill rejection and distributions of several kinematic variables were compared between them; see 4.8.

Table 4.8: Runs chosen for comparison

| Run | Number of spills | Rejected spills | Percentage |
|---|---|---|---|
| 297 482 | 190 | 6 | 3.16% |
| 297 484 | 189 | 39 | 20.63% |
| 297 487 | 197 | 33 | 16.75% |

The $\chi^2$ test was used to compare histograms of several variables between the listed runs. The histograms were expected to become more compatible after the bad spills of each run were removed from the analysis.

Table 4.9 shows the p-value of the $\chi^2$ test before performing any event selection or further cuts.

Table 4.9: $\chi^2$ comparison of variables before cuts

| | | 297482 297484 | 297482 297487 | 297484 297487 |
|---|---|---|---|---|
| $Q^2$ | with BS | $3.06{\cdot}10^{-5}$ | $1.30{\cdot}10^{-5}$ | 0.135 |
| | without BS | 0.050 | 0.279 | 0.066 |
| $x$ | with BS | 0.458 | 0.746 | 0.464 |
| | without BS | 0.688 | 0.776 | 0.629 |
| $W$ | with BS | 0.557 | 0.359 | 0.550 |
| | without BS | 0.866 | 0.644 | 0.583 |
| $y$ | with BS | 0.123 | 0.017 | 0.806 |
| | without BS | 0.358 | 0.050 | 0.665 |
| $z$ | with BS | 0.145 | 0.061 | 0.473 |
| | without BS | 0.046 | 0.134 | 0.397 |
| $l_x$ | with BS | $2.95{\cdot}10^{-78}$ | $7.28{\cdot}10^{-209}$ | $6.18{\cdot}10^{-18}$ |
| | without BS | $2.14{\cdot}10^{-74}$ | $1.35{\cdot}10^{-203}$ | $4.74{\cdot}10^{-16}$ |
| $l_y$ | with BS | $7.33{\cdot}10^{-7}$ | $7.96{\cdot}10^{-19}$ | 0.152 |
| | without BS | $1.47{\cdot}10^{-9}$ | $5.26{\cdot}10^{-27}$ | 0.116 |
| $l_z$ | with BS | $1.95{\cdot}10^{-6}$ | $1.78{\cdot}10^{-19}$ | 0.010 |
| | without BS | 0.026 | $7.33{\cdot}10^{-12}$ | 0.028 |
| $l'_x$ | with BS | 0.552 | 0.063 | 0.232 |
| | without BS | 0.436 | 0.063 | 0.128 |
| $l'_y$ | with BS | $1.60{\cdot}10^{-4}$ | $2.89{\cdot}10^{-5}$ | 0.017 |
| | without BS | 0.133 | 0.013 | 0.084 |
| $l'_z$ | with BS | 0.035 | 0.130 | 0.831 |
| | without BS | 0.369 | 0.291 | 0.867 |
| $\phi_{\mu 0}$ | with BS | $3.32{\cdot}10^{-4}$ | $5.28{\cdot}10^{-18}$ | 0.002 |
| | without BS | 0.002 | $1.33{\cdot}10^{-15}$ | 0.003 |
| $\phi_{\mu}$ | with BS | 0.085 | 0.079 | 0.039 |
| | without BS | 0.203 | 0.074 | 0.044 |
| $\lvert \boldsymbol{P}_{hT} \rvert$ | with BS | 0.097 | 0.592 | 0.139 |
| | without BS | 0.155 | 0.616 | 0.191 |

Some of the compared variables were plotted, both with bad spills and without, as an example. Figure 4.11 compares $W$ between runs 297482 and 297484. In this case, the p-value significantly increased, which is the desired outcome.

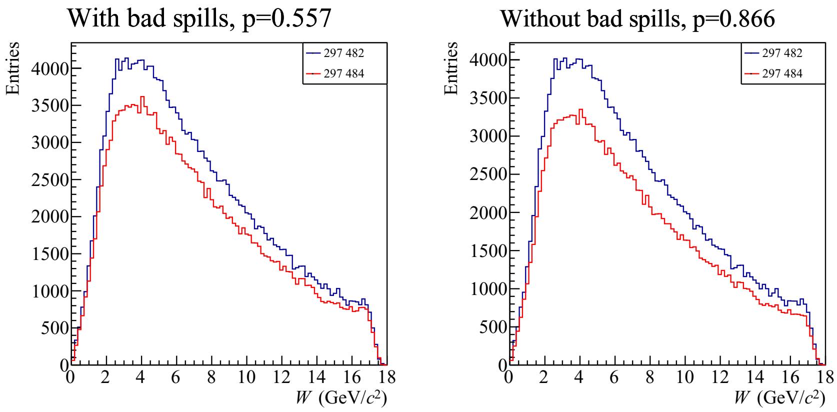

Figure 4.11: $W$ comparison for runs 297482 and 297484

However, in some cases, the p-value of the $\chi^2$ test behaved precisely the opposite way. This is the case of 4.12, where the p-value decreases. This is not surprising, as the beam drifts slightly over time. It is also possible that these runs might have additional issues and might be thus removed during the later stage of the analysis, the so-called bad run analysis.

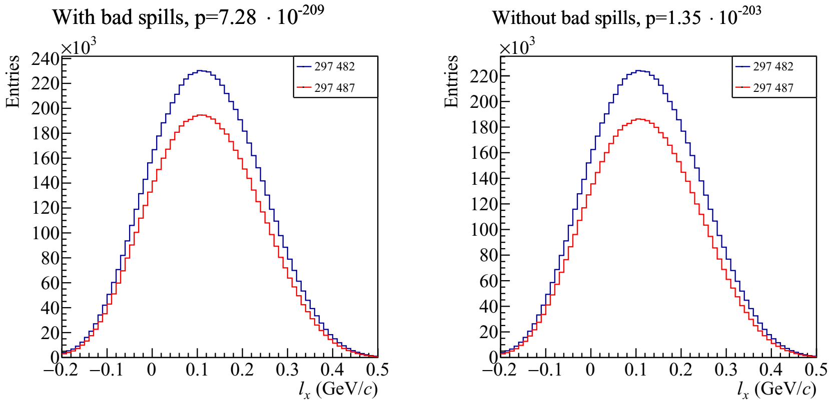

Figure 4.12: $l_x$ comparison for runs 297482 and 297487

In other cases, the p-value remained approximately the same as the $|\boldsymbol{P}_{hT}|$ variable between runs 297482 and 297487.

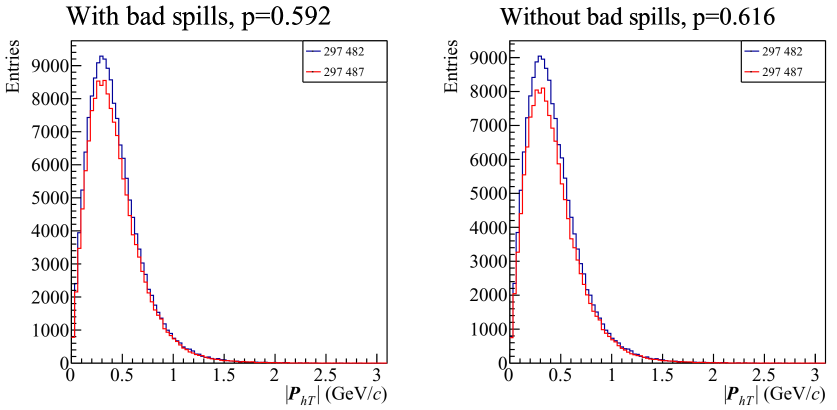

Figure 4.13: $|\boldsymbol{P}_{hT}|$ comparison for runs 297482 and 297487

Before the event selection, a total number of 14 p-values increased, 6 decreased, and in 22 cases, the p-value remained roughly the same.

Implementing event selection was expected to lead to further enhancements in the results. The list of chosen criteria follows [22]:

- **Cuts on the primary vertex**, which has to be considered best by PHAST. That is determined by the vertex $\chi^2$ and the number of outgoing particles.
    - the primary vertex has to be inside the target (selected by PHAST PaAlgo::InTarget())
- **Cuts on the beam $\mu$**
    - muon momentum: $140 < P_\mu/(\mathrm{GeV}/c) < 180$
    - reduced $\chi^2 < 10$
    - the beam crosses the whole target (checked by PaAlgo::CrossCells)
- **Cuts on the scattered muon $\mu'$**
    - first hit $Z_{First} < 350$ cm
    - reduced $\chi^2 < 10$
    - scattered muon has to be only one and identified with the iMuPrim function
    - ambiguous tracks with the same charge as muon are rejected
    - last hit $Z_{Last} > 33$ m
- **Kinematic cuts**
    - $Q^2 > 1\ (\mathrm{GeV}/c)^2$
    - $W > 5\ (\mathrm{GeV}/c^2)$
    - $0 < x < 1$
    - $0.1 < y < 0.9$
- **Cuts on the outgoing tracks except of $\mu'$**
    - number of radiation lengths $X/X_0 < 10$
    - reduced $\chi^2 < 10$
    - first hit $Z_{First} < 350$ cm
    - last hit $Z_{Last} > 350$ cm
    - $0.1 < z < 0.9$
    - $0.1 < |\boldsymbol{P}_{hT}|/(\mathrm{GeV}/c) < 2.0$

After selecting the suitable events, the variables were again compared by the $\chi^2$ test. Table 4.10 shows the resulting values.

Table 4.10: $\chi^2$ comparison of variables

| | | 297482 297484 | 297482 297487 | 297484 297487 |
|---|---|---|---|---|
| $Q^2$ | with BS | 0.516 | 0.844 | 0.218 |
| | without BS | 0.115 | 0.796 | 0.107 |
| $x$ | with BS | 0.549 | 0.613 | 0.557 |
| | without BS | 0.697 | 0.694 | 0.625 |
| $W$ | with BS | 0.741 | 0.640 | 0.797 |
| | without BS | 0.932 | 0.515 | 0.756 |
| $y$ | with BS | 0.337 | 0.548 | 0.628 |
| | without BS | 0.388 | 0.563 | 0.702 |
| $z$ | with BS | 0.013 | 0.055 | 0.068 |
| | without BS | 0.010 | 0.059 | 0.154 |
| $l_x$ | with BS | 0.648 | 0.087 | 0.384 |
| | without BS | 0.916 | 0.081 | 0.558 |
| $l_y$ | with BS | 0.489 | 0.226 | 0.376 |
| | without BS | 0.608 | 0.246 | 0.265 |
| $l_z$ | with BS | 0.391 | 0.237 | 0.175 |
| | without BS | 0.543 | 0.519 | 0.269 |
| $l'_x$ | with BS | 0.507 | 0.995 | 0.730 |
| | without BS | 0.740 | 0.992 | 0.868 |
| $l'_y$ | with BS | 0.686 | 0.468 | 0.422 |
| | without BS | 0.736 | 0.306 | 0.596 |
| $l'_z$ | with BS | 0.033 | 0.396 | 0.054 |
| | without BS | 0.024 | 0.336 | 0.103 |
| $\phi_{\mu 0}$ | with BS | 0.177 | 0.111 | 0.682 |
| | without BS | 0.211 | 0.125 | 0.613 |
| $\phi_\mu$ | with BS | 0.792 | 0.486 | 0.565 |
| | without BS | 0.657 | 0.322 | 0.354 |
| $\lvert \boldsymbol{P}_{hT} \rvert$ | with BS | 0.066 | 0.051 | 0.068 |
| | without BS | 0.084 | 0.086 | 0.102 |

Figure 4.14 presents results for $W$ after applying the list of cuts on the processed data. The cuts led to further improvement for both the p-values.

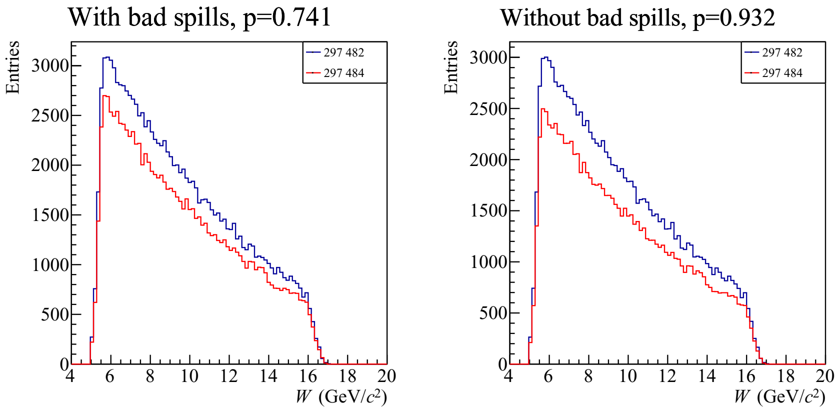
With bad spills, p=0.741

Without bad spills, p=0.932

Figure 4.14: $W$ comparison for runs 297482 and 297484

The results are much better for $l_x$, where the results increased significantly for comparison with and without bad spills. Even better is that the relative difference between the two p-values decreased greatly, see 4.15.

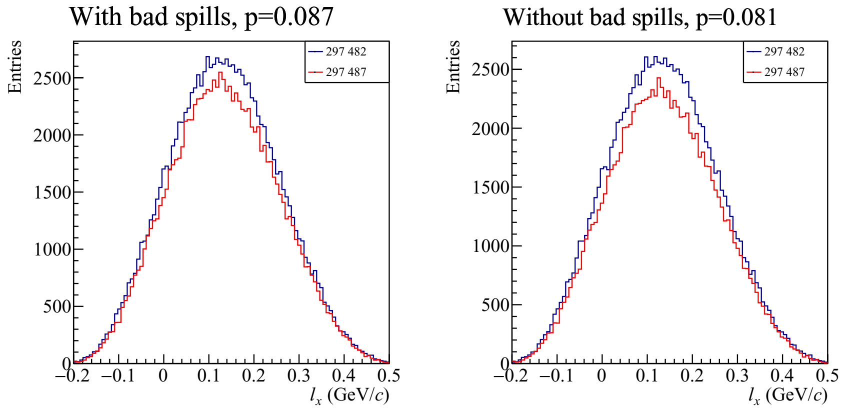

Figure 4.15: $l_x$ comparison for runs 297482 and 297487

Before the implementation of the cuts, the p-values were almost identical for $\boldsymbol{P}_{hT}$ (see 4.13). Now, the p-value for the plot without the bad spills is almost twice the p-value of the plot with the bad spills. However, it is also important to point out that both p-values decreased significantly but are still considered reasonable.

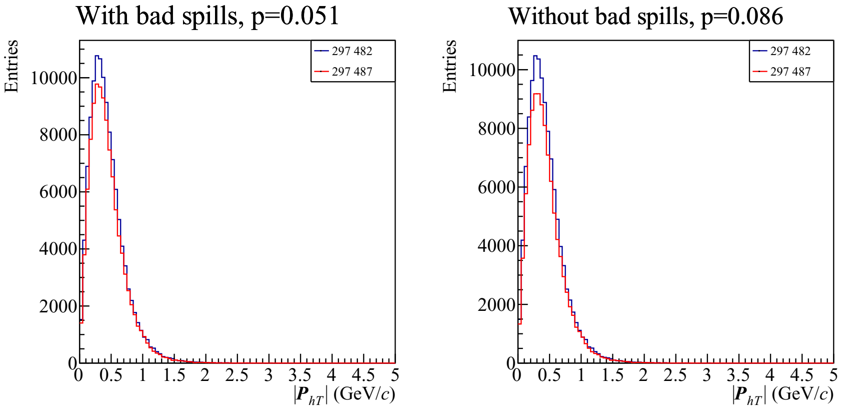

Figure 4.16: $|\boldsymbol{P}_{hT}|$ comparison for runs 297482 and 297487

In total, the resulting p-value improved in 14 cases, got worse in 7 cases and remained approximately the same in 21 cases.

# Conclusion

The transverse momentum dependent (TMD) functions are an extension of the parton model. To this day, extracting them is one of the most challenging tasks in hadron physics. One of the possible methods of measuring these functions is studying the semi-inclusive DIS and measuring the transverse spin asymmetries. Along with, for example, the HERMES experiment and Jefferson labs experiments, the COMPASS Collaboration is one of the key experiments in the field and has already provided results strongly supporting the TMD framework [6, 23].

This thesis presents results for the polarised target analysis, in which the coordinates of the target's axis and target cells were determined and updated in the PHAST function for 2022 data. Further, the homogeneity of the target density was checked using distributions of vertices and beam tracks in the target.

The second part of the thesis focuses on the bad spill analysis. It describes the algorithm used to mark outliers among the spills and two methods of dealing with "bad spill island". Results from two periods of 2022 data-taking are presented, namely W03t1 and W07t2. The analysis revealed a rejection rate of about 16% for W03t1 and 7% for W07t2. These rejection rates are comparable to data collected in previous years, showing a reasonable quality of collected data. At the end of the chapter, several runs from the W07t2 period are compared, and the effect of the bad spill rejection is examined. The comparison of three randomly chosen runs from period W07t2 suggests that bad spill analysis results in more compatible data, specifically the p-value before the event selection increased in 14 cases and decreased in 6 cases, and improved in 14 cases and decreased in 7 cases after the event selection. In the rest of the cases, the p-value remained approximately the same.

# Bibliography

[1] David J Griffiths. *Introduction to elementary particles; 2nd rev. version.* Physics textbook. Wiley, New York, NY, 2008.

[2] The SLAC-MIT experiment. NobelPrize.org. Nobel Prize Outreach AB 2023. Tue. 25 Apr 2023. `https://www.nobelprize.org/prizes/physics/1990/9594-the-slac-mit-experiment/`.

[3] COMPASS conference talks and proceedings, `http://wwwcompass.cern.ch/compass/publications/talks/`.

[4] Vincenzo Barone, Alessandro Drago, and Philip G. Ratcliffe. Transverse polarisation of quarks in hadrons. *Physics Reports*, 359(1):1–168, 2002.

[5] Heiner Wollny. *Measuring azimuthal asymmetries in semi-inclusive deep-inelastic scattering off transversely polarized protons.* PhD thesis, Universität Freiburg, 2010.

[6] Andrea Moretti. *Transversity and $\Lambda$ polarisation in polarised SIDIS.* PhD thesis, University of Trieste, 2017.

[7] Robin Devenish and Amanda Cooper-Sarkar. Deep Inelastic Scattering. Oxford University Press, 11 2003.

[8] Jiří Chýla. *Quarks, partons and Quantum Chromodynamics.* Published online, 2009. `https://www.fzu.cz/~chyla/lectures/text.pdf`.

[9] Alessandro Bacchetta, Markus Diehl, Klaus Goeke, Andreas Metz, Piet J Mulders, and Marc Schlegel. Semi-inclusive deep inelastic scattering at small transverse momentum. *Journal of High Energy Physics*, 2007(02):093–093, feb 2007.

[10] April Townsend. *Transverse single-spin asymmetries in pion-induced Drell-Yan and $J/\Psi$ production at COMPASS.* PhD thesis, University of Illinois, 2022.

[11] Michael Pešek. *Pion-induced polarized Drell-Yan process at COMPASS.* PhD thesis, Charles University, 2020.

[12] M. Tanabashi et al. Review of particle physics. *Phys. Rev. D*, 98:030001, Aug 2018.

[13] Albi Kerbizi. *Recursive fragmentation of a polarized quark.* PhD thesis, University of Trieste, 2019.

[14] M. Radici, A. Courtoy, A. Bacchetta, and M. Guagnelli. Improved extraction of valence transversity distributions from inclusive dihadron production. JHEP, 05, 123, 2015.

[15] M. Anselmino, M. Boglione, U. D'Alesio, F. Murgia, and A. Prokudin. Study of the sign change of the sivers function from STAR collaboration w/z production data. *Journal of High Energy Physics*, 2017(4), apr 2017.

[16] P. Abbon et al. The compass experiment at cern. *Nuclear Instruments and Methods in Physics Research Section A: Accelerators, Spectrometers, Detectors and Associated Equipment*, 577(3):455–518, 2007. `https://www.sciencedirect.com/science/article/pii/S0168900207005001`.

[17] CERN. Compass, 2023. `https://wwwcompass.cern.ch`.

[18] COMPASS colaboration. Compass, 2023. `https://home.cern/science/experiments/compass`.

[19] Maria Grazia Pia and Georg Weidenspointner. Monte carlo simulation for particle detectors, 2012.

[20] Rene Brun and Fons Rademakers. Root - an object oriented data analysis framework, 1997. URL `https://root.cern`.

[21] Physics analysis software tools of compass. URL `http://ges.web.cern.ch/ges/phast/index.html`.

[22] F. Bradamante et al. Results on azimuthal asymmetries and $p_t^2$-dependent distributions for charged hadrons from 2016 data. 2020.

[23] Jan Matoušek. *Nucleon spin structure studies in Drell-Yan process at COMPASS*. PhD thesis, Charles University, University of Trieste, 2018.

# List of Figures

# List of Tables

# List of Abbreviations

- **COMPASS** - COmmon Muon Proton Apparatus for Structure and Spectroscopy
- **CORAL** - COMPASS reconstruction and analysis
- **DAQ** - Data Acquisition
- **DCS** - Detector Control System
- **DIS** - Deep inelastic scattering
- **ECAL** - Electromagnetic Calorimeter
- **GNS** - Gamma-Nucleon System
- **HCAL** - Hadronic Calorimeter
- **IT** - Inner Trigger
- **LAST** - Large Angle Spectrometer Trigger
- **LAT** - Large Area Trackers
- **LT** - Ladder Trigger
- **mDST** - mini Data Summary Tape
- **MT** - Middle Trigger
- **MW1/MW2** - Muon Wall 1/2
- **OT** - Outer Trigger
- **PDF** - Parton Distribution Function
- **PHAST** - PHysics Analysis Software Tools
- **RICH** - Ring Imaging Cherenkov
- **RMS** - Root Mean Square
- **SAT** - Small Area Trackers
- **SIDIS** - Semi inclusive deep inelastic scattering
- **SPS** - Super Proton Synchrotron
- **TMD-PDF** - Transverse Momentum Dependent Parton Distribution Function
- **VSAT** - Very Small Area Trackers